AD_____

Award Number: W81XWH-12-1-0522

TITLE: Development and Testing of Iron Based Phantoms as Standards for the Diagnosis of Microbleeds and Oxygen Saturation with Applications in Dementia, Stroke, and Traumatic Brain Injury

PRINCIPAL INVESTIGATOR: Yu-Chung Norman Cheng

CONTRACTING ORGANIZATION: Wayne State University
                          DETROIT, MI 48201

REPORT DATE: October 2014

TYPE OF REPORT: Annual Report

PREPARED FOR: U.S. Army Medical Research and Materiel Command
              Fort Detrick, Maryland 21702-5012

DISTRIBUTION STATEMENT: Approved for Public Release;
                        Distribution Unlimited

REPORT DOCUMENTATION PAGE

1. REPORT DATE October 2014	2. REPORT TYPE Annual Report	3. DATES COVERED 29 Sep. 2013 – 29 Sep. 2014	
4. TITLE AND SUBTITLE Development and Testing of Iron Based Phantoms as Standards for the Diagnosis of Microbleeds and Oxygen Saturation with Applications in Dementia, Stroke, and Traumatic Brain Injury		**5a. CONTRACT NUMBER**	
		5b. GRANT NUMBER W81XWH-12-1-0522	
		5c. PROGRAM ELEMENT NUMBER	
6. AUTHOR(S) Yu-Chung Norman Cheng E-Mail: yxc16@wayne.edu		**5d. PROJECT NUMBER**	
		5e. TASK NUMBER	
		5f. WORK UNIT NUMBER	
7. PERFORMING ORGANIZATION NAME(S) AND ADDRESS(ES) Wayne State University Detroit, Michigan, 48202		**8. PERFORMING ORGANIZATION REPORT NUMBER**	
9. SPONSORING / MONITORING AGENCY NAME(S) AND ADDRESS(ES) U.S. Army Medical Research and Materiel Command Fort Detrick, Maryland 21702-5012		**10. SPONSOR/MONITOR'S ACRONYM(S)**	
		11. SPONSOR/MONITOR'S REPORT NUMBER(S)	

12. DISTRIBUTION / AVAILABILITY STATEMENT
Approved for Public Release; Distribution Unlimited

13. SUPPLEMENTARY NOTES

14. ABSTRACT
As our project was suspended since the fifth quarter due to insufficient funds in this second year, here we will report our findings during the fifth quarter. Nonetheless, we still have some potable outcomes to report toward the end of this report. We have now understood better about the slight disagreements or inconsistencies between CISSCO results and phase values inside straws. The problem is due to interactions between particles (or molecules) and water. From the past literature, this is called hyperfine shifts in NMR studies. All of our re-analyzed results from gadolinium and ferritin solutions are consistent between different echo times from MRI measurements, but results from calcium solutions remain inconsistent. In fact, results from calcium solutions do not seem repeatable. This may be due to very high concentrations of calcium solutions (at least 5% in volume). CISSCO results from low concentration nanoparticle solutions also agree with phase values inside straws but accuracies become an issue. Also in the fifth quarter, from a phantom study with one straw in the phantom, we have compared results from CISSCO, SWIM, and a quantitative susceptibility mapping (QSM) method from the Cornell group. Results from CISSCO are consistent and accurate but results from SWIM and Cornell QSM are not. Lastly, we have applied the 3D CISSCO method for the susceptibility quantifications of some air bubbles and glass beads.

15. SUBJECT TERMS
  MRI, susceptibility quantification, gel phantoms, simulated brain images, numerical models, nanoparticles, gadolinium, ferritin, calcium, multiple concentrations, multiple echo times,

16. SECURITY CLASSIFICATION OF:			17. LIMITATION OF ABSTRACT	18. NUMBER OF PAGES	19a. NAME OF RESPONSIBLE PERSON USAMRMC
a. REPORT U	**b. ABSTRACT** U	**c. THIS PAGE** U	UU	28	**19b. TELEPHONE NUMBER** *(include area code)*

Table of Contents

INTRODUCTION

Magnetic resonance imaging (MRI) offers a powerful, non-invasive means to image the human body. Recent advances in imaging the brain have led to the potential of monitoring iron build up, blood products in dementia, stroke, traumatic brain injury, and the measurement of oxygen saturation. These advances relate directly to both monitoring and measuring the amount of iron in brain tissues that have changes in magnetic susceptibility of each individual tissue. Therefore, the proper quantification of mineral such as iron will play a key role in future radiology practice. While a number of groups using several methods are approaching this topic, the current problems are that no standard protocol has been established nor sensitivities and uncertainties of these methods have been properly evaluated. These methods include the background phase removal techniques. Without the standard protocol or understanding of uncertainties of developed methods, the quantified susceptibility values can be questionable. As a first step, we want to establish a standard protocol with accurate methods for the magnetic susceptibility quantifications of materials in phantoms. In this second year, we have accurately quantified susceptibilities of several concentrations of three different materials in water and gel with MRI, using phase values outside the straws which different solutions with materials were filled in. However, phase values inside some of those straws did not lead to consistent results. Further analyses reveal additional frequency shifts due to interactions between materials and their surroundings (the so-called hyperfine shifts). The detailed methods and results are presented below.

BODY

A. Consistencies between susceptibility measurements from CISSCO and phase values inside straws

One unsolved problem from the first year has been that the susceptibility values quantified from our CISSCO (Complex Image Summation around a Spherical or a Cylindrical Object) method [Cheng et al., 2009], do not fully agree with the values calculated from direct phase measurements inside straws (containing different concentrations of materials). For the direct phase measurement inside each straw, we simply record the phase value from the central pixel in the straw. As many of the discrepancies are not large in terms of phase values (but above the white noise level), we have first spent a great deal of time to investigate whether the problem is due to some systematic errors in SHARP or due to the Gibbs ringing or partial volume effect. The former is discussed in more details below, but it is not sufficient to explain those discrepancies from ferritin solutions. The latter, from many simulations including two different ideas of calculating the phase value inside a straw, does not seem to affect the phase value in the middle of the straw by more than 0.1 radian. This is perhaps expected, as the radius of each straw is about 3 pixels in images, Gibbs ringing effect is too small to notice.

This prompted us to review couple old papers [Chu et al., 1990; Fossheim et al., 1996], which explains additional frequency shifts in NMR due to interactions between particles/molecules and their surrounding (e.g., water). These additional frequency shifts will not affect phase values outside the materials (and thus outside the straws in our cases), as the phase values outside the materials are considered to be from the magnetic susceptibility effect. With the consideration of these interactions, we re-analyze our gadolinium and ferritin phantoms and present our results below. In general, this new consideration leads to agreements between CISSCO results and direct phase measurements.

1) Simulations of effects from the combination of FSL and SHARP

To understand the effects from the phase unwrapping and background removal methods, we applied prelude (FSL) algorithm and SHARP [Schweser et al, 2011] on simulated images. We simulated a cylindrical object on 4096 x 4096 images. Through Fourier transformation, the targeted radius of the cylindrical object was 3 pixels on 256 x 256 images. The object was also inside a round region with a background phase of 2 radians. The axis of the cylinder was arranged to be perpendicular to the main field with a strength of 2.89 T. Fifteen magnetic moment values were assigned to the object such that phase values inside and outside the cylinder were also simulated. Applying FSL to unwrap the simulated phase patterns, and then SHARP to remove the background phase, we were able to quantify the magnetic moment of each simulation with CISSCO. The results of the moment values after these procedures were compared with the input values (see Fig. 1).
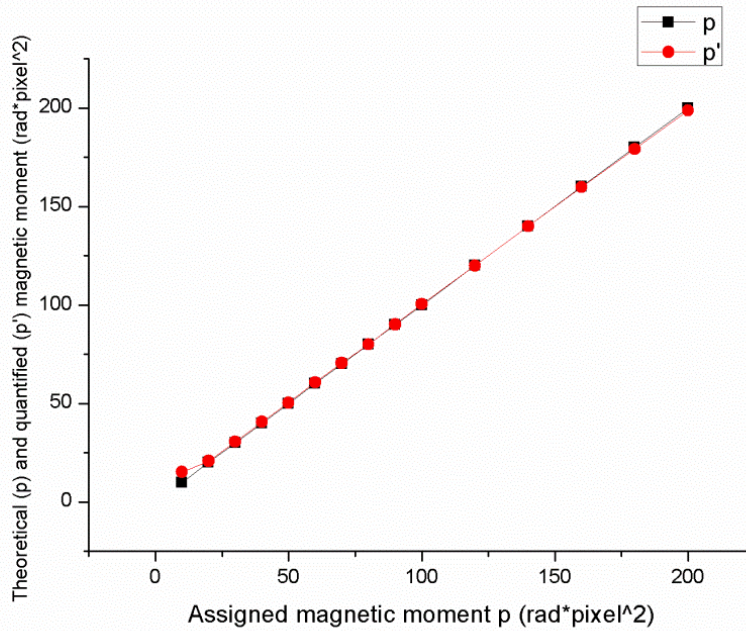
Figure 1: Theoretical magnetic moments versus quantified values from CISCCO after the applications of FSL and SHARP. The symbol *p* refers to the theoretical (or input) magnetic moments. The symbol *p'* refers to quantified magnetic moments from CISSCO.

From Fig. 1, FSL combined with SHARP leads to reliable quantified results in the range of consideration, as long as the magnetic moments are not very small (below 20 rad·pixels^2). For small moment values, insufficient phase outside the object can lead to large errors in the quantification.

Furthermore, we examined the phase values inside the cylindrical objects. We directly measured the phase values after unwrapping phase with FSL and measured the phase again after the application of SHARP. These results and theoretical phase values calculated from the input magnetic moments are shown in Fig. 2. Note that these phase values have been unwrapped so they were not confined within $-\pi$ and π. In addition, the phase results after applying FSL and SHARP may differ from the true phase values by $2n\pi$, where n is an arbitrary integer. As we roughly know the correct phase values, we have manually made such corrections. In addition, for comparison purposes, the known background phase, 2 radians, has been subtracted from the unwrapped phase values after FSL. After these additional minor procedures, we can compare and plot those phase values with theoretical magnetic moments.
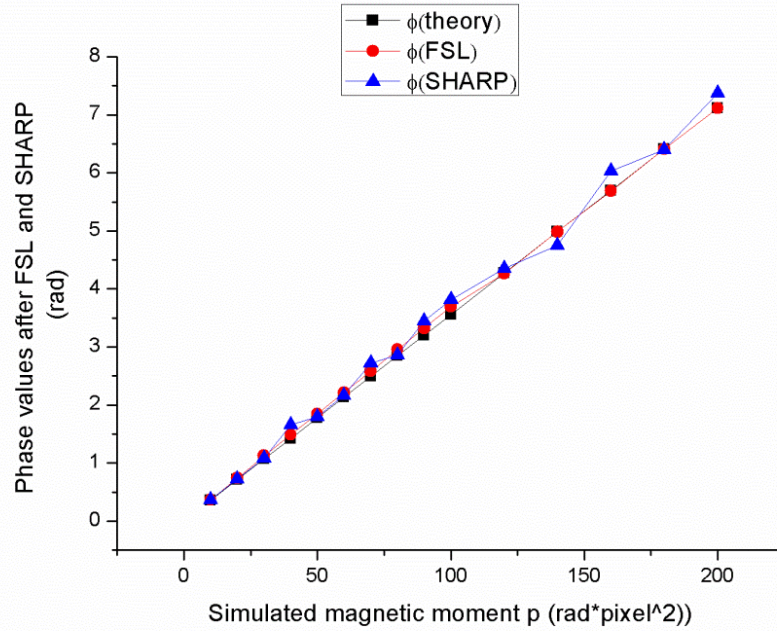
Figure 2: Relations between the phase value inside each simulated cylinder, after the applications of FSL and SHARP, versus the magnetic moment of the simulated cylinder. The simulated cylinders are perpendicular to the main field. The theoretical relation between the two variables is shown by the black squares (ϕ(theory)). The relation based on the measured phase values after only using FSL is shown by red disks (ϕ(FSL)). The relation based on the measured phase values after using both FSL and SHARP is shown by blue triangles (ϕ(SHARP)).

In Fig. 2, measured phase values after using only FSL agree well with the theoretical values. However, measured phase values after using FSL and SHARP show differences from some theoretical values. These differences depend on both the actual phase value and the unwrapped phase values from FSL. The largest difference from our simulation can be up to 5% of the theoretical value. These results can be considered as a systematic error when we compare the CISSCO results to the direct phase measurements. However, 5% of 7 radians (which is roughly the largest phase value inside our straws) is only 0.35 radian. This 0.35 radian is not large enough to explain the observed differences between direct phase measurements and magnetic moment measurements from actual phantom images. Thus we discuss a different possibility in the next subsection.

After the applications of FSL and SHARP, we note a standard deviation of roughly 0.07 radian on phase images inside the phantom. This standard deviation will be used for uncertainty estimations below.

2) Frequency shifts due to particle/molecule interactions with water

Chu et al, 1990 and Fossheim et al., 1996 state that interactions between particles or molecules with water can lead to frequency shifts in MR spectroscopy. These shifts as well as the susceptibility effect will affect the precession of proton spins and thus change phase values inside straws of our phantoms. On the other hand, phase distributions outside the straws would be only affected by the susceptibility effect. As our CISSCO method utilizes the phase values outside each straw for the quantification of the magnetic moment, we can assume that CISSCO provides us the correct susceptibility value (but the direct measurements of phase values inside straws do not).

We can write down the relation between the phase value inside a cylindrical object (φ_{in}) and the magnetic moment p quantified from CISSCO (from the perpendicular orientation). Given the convention of phase definition in Siemens MRI systems, we have

$$\varphi_{in} = p \, (3 \cos^2\theta - 1) \, / \, (3a^2) + \varphi_f \qquad [1]$$

6

where θ is the angle between the axis of the cylinder and the main field, a is the radius of the cylinder, and φ_f is the phase term due to the interactions. Note that φ_f is independent of the orientation of the cylinder and only affects the phase value inside the cylinder. However, as φ_f is based on the frequency shift, φ_f should still be proportional to the echo time TE.

With phase measurements from both parallel and perpendicular orientation, we can rewrite Eq. 1 as

$$p = (\varphi_{par} - \varphi_{per})\, a^2 \qquad\qquad [2]$$

where φ_{par} is the measured phase value inside the cylinder at the parallel orientation ($\theta = 0°$) and φ_{per} is the measured phase value inside the cylinder at the perpendicular orientation ($\theta = 90°$).

We have used two Vernier calibers to carefully measure the diameter of the straws we use. We obtain $2a = 5.97 \pm 0.06$ mm. Given the one standard deviation of 0.07 radian induced by FSL and SHARP in phase images, we can estimate the uncertainty on the right hand side of Eq. 2, based on these numbers and the error propagation method. These uncertainties are labeled as δp in Tables 1, 2, and 3 below.

We can also derive φ_f from Eq. 1

$$\varphi_f = (\varphi_{par} + 2\varphi_{per}) / 3 \qquad\qquad [3]$$

The uncertainty of φ_f (one standard deviation) is about 0.052 radian for all quantifications. Thus, in the following discussions, only when φ_f is larger than 0.1 radian (two standard deviations) is worth our attention about this interaction term.

a) Results from Gd-DPTA phantoms

We re-analyzed the images using Eqs. 1-3 from our Gd-DPTA phantoms with the applications of FSL and SHARP. The results are listed in Table 1 below.

No.	TE (ms)	p (rad·pexel^2)	φ_{per} (rad)	φ_{par} (rad)	p' (rad·pexel^2)	Δp (%)	δp (%)	φ_f (rad)
1		54.79	-1.90	4.09	53.19	-3.00	3.67	0.10
2	8.07	27.81	-0.94	2.16	27.53	-1.02	5.23	0.09
3		14.37	-0.66	1.08	15.45	7.00	7.75	-0.08
4		10.02	-0.40	0.58	8.70	-15.14	12.20	-0.07
1		72.00	-2.48	5.23	68.47	-5.16	3.30	0.09
2	10.46	36.14	-1.25	2.69	34.99	-3.29	4.54	0.06
3		18.67	-0.86	1.44	20.42	8.59	6.35	-0.09
4		8.43	-0.51	0.74	11.10	24.06	10.00	-0.09
1		87.44	-3.27	6.47	86.50	-1.09	3.03	-0.02
2	12.85	43.19	-1.63	3.31	43.87	1.55	4.02	0.02
3		22.69	-1.02	1.74	24.51	7.43	5.62	-0.10
4		12.59	-0.58	0.94	13.50	6.73	8.58	-0.07
1		102.56	-3.78	7.58	100.88	-1.66	2.88	0.01
2	15.24	51.97	-1.85	3.96	51.60	-0.73	3.72	0.09
3		26.87	-1.15	2.09	28.77	6.61	5.09	-0.07
4		13.56	-0.61	1.10	15.19	10.70	7.85	-0.04
1		119.58	-4.40	8.84	117.58	-1.70	2.76	0.01
2	17.63	59.60	-2.17	4.50	59.23	-0.62	3.50	0.05
3		30.85	-1.25	2.39	32.32	4.56	4.75	-0.04
4		15.15	-0.65	1.27	17.05	11.15	7.21	-0.01
1		187.64	-7.09	14.73	193.77	3.16	2.46	0.18
2	29.58	96.18	-3.93	7.68	103.10	6.71	2.86	-0.06
3		50.18	-1.99	4.10	54.08	7.21	3.64	0.04
4		24.00	-1.11	2.16	29.04	17.35	5.06	-0.02

Table 1: Magnetic moment and phase measurements and their comparisons from a gadolinium phantom. The first column labels the straw. The second column lists the echo time, as the phantoms were imaged by an 11-echo SWI (susceptibility weighted imaging) sequence. The third column lists the magnetic moment p quantified from CISSCO. The fourth column (φ_{per}) lists the measured phase value inside each straw at the perpendicular orientation. The fifth column (φ_{par}) lists the measured phase value inside each straw at the parallel orientation. The sixth column (p') lists the values calculated from Eq. 2. The seventh column (Δp) lists the percentage differences between p and p'. The eighth column (δp) lists the percentage uncertainties calculated from Eq. 2, as described in the text. The ninth column lists the estimated φ_f values.

We should first pay attention to whether $|\Delta p|$ is no more than two standard deviations of δp (i.e., $2\,\delta p$). In usual scientific discussions, when the difference between two numbers is within the two standard deviations of the uncertainty, then we can say that we have an agreement between these two numbers. Except for results from TE = 29.58 ms and the results of the 4th straw at TE = 10.46 ms, all other comparisons satisfy $|\Delta p| <= 2\,\delta p$. The value of $|\Delta p|$ of the 4th straw at TE = 10.46 ms is within $3\,\delta p$ and this can be considered "normal" among 20 measurements. The uncertainty of quantified moment p from CISSCO is especially large when $p < 20$ rad·pixels^2, as stated above.

The problem at TE = 29.58 ms requires a closer check. We find out that the susceptibility values calculated from the third column in Table 1 are generally smaller than the susceptibility values calculated from other shorter echo times. In fact, we observe the same trend for the ferritin, calcium, and nanoparticle phantoms. This indicates that there is still some systematic error introduced by FSL/SHARP, even though simulated results shown in Fig. 1 do not suggest such an error. If we use the quantified susceptibility values from shorter echo times to estimate the magnetic moment p at TE = 29.58 ms, we actually will have $|\Delta p| <= 2\,\delta p$. Thus, we can conclude that MRI measurements from gadolinium are self-consistent.

For the interaction term φ_f, only the value from the first straw at TE = 29.58 ms is more than 0.1 radian. However, this again is likely due to the systematic error introduced by FSL/SHARP, as shown in Fig. 2. Thus, we can also conclude that gadolinium do not show noticeable interactions with water. This agrees with the results from [Fossheim et al., 1996].

b) Results from ferritin phantoms

We also re-analyze our ferritin phantoms with the same procedures. The results are listed in Table 2.

No.	TE (ms)	p (rad·pexel^2)	φ_{per} (rad)	φ_{par} (rad)	p' (rad·pexel^2)	Δp (%)	δp (%)	φ_f (rad)
1		76.17	-2.54	5.61	72.38	-4.98	3.23	0.18
2	8.07	37.97	-1.54	2.91	39.52	3.92	4.25	-0.06
3		18.95	-0.71	1.48	19.45	2.56	6.57	0.02
4		9.53	-0.33	0.80	10.03	5.03	10.85	0.05
1		99.36	-3.55	7.34	96.71	-2.67	2.92	0.08
2	10.46	49.81	-1.95	3.82	51.24	2.79	3.73	-0.03
3		24.77	-0.91	1.94	25.31	2.13	5.51	0.04
4		12.44	-0.43	1.08	13.41	7.23	8.62	0.07
1		121.69	-3.98	8.91	114.47	-5.93	2.78	0.32
2	12.85	60.87	-2.44	4.69	63.32	3.87	3.40	-0.06
3		29.48	-1.14	2.38	31.26	5.69	4.84	0.03
4		15.11	-0.55	1.26	16.07	5.99	7.52	0.05
1		275.99	-9.45	20.77	268.37	-2.76	2.33	0.62
2	29.58	139.63	-5.69	10.74	145.90	4.30	2.61	-0.21
3		67.48	-2.87	5.55	74.77	9.75	3.19	-0.06
4		33.69	-1.37	2.86	37.56	10.31	4.36	0.04

Table 2: Magnetic moment and phase measurements and their comparisons from a ferritin phantom. The notations and meanings of each column have been explained in the caption of Table 1.

Similar to the gadolinium phantom, p and p' values of ferritin have also showed good agreements except for those at the longest echo time. Scaling the magnetic moments by susceptibility values from shorter echo times will also reduce Δp to within $2\, \delta p$. Thus, we can conclude that MRI measurements from ferritin are also self-consistent.

However, from the φ_f values, the ferritin solution inside the first straw clearly shows interactions between ferritin and water. These results indicate that the frequency shifts due to interactions had affected our previous phase measurements, when we compared CISSCO results to φ_{per}.

c) Results from nanoparticle phantoms

We re-analyze some of our nanoparticle phantoms with the same procedures. In order to show some anomalies, we present a few results in Table 3.

No.	TE (ms)	p (rad·pexel^2)	φ_{per} (rad)	φ_{par} (rad)	p' (rad·pexel^2)	Δp (%)	δp (%)	φ_f (rad)
1		32.62	2.76	0.23	22.47	-31.12	5.95	1.92
2	8.07	16.28	-1.59	0.2	15.90	-2.36	7.59	-0.99
3		8.28	-0.69	0.18	7.73	-6.69	13.49	-0.40
4		7.39	-0.28	0.14	3.73	-49.53	25.81	-0.14
1		52.12	0.73	0.48	2.22	-95.74	42.00	0.65
2	12.85	26.33	-2.46	0.38	25.22	-4.21	5.52	-1.51
3		14.12	-1.07	0.3	12.17	-13.84	9.30	-0.61
4		6.77	-0.45	0.32	6.84	1.00	14.99	-0.19

Table 3: Magnetic moment and phase measurements and their comparisons from a nanoparticle phantom. The notations and meanings of each column have been explained in the caption of Table 1.

We first observe that only results from the first straw do not satisfy $|\Delta p| \leq 2\, \delta p$. However, we should note that the quantified magnetic moments from the third and the fourth straw are less than 20 rad·pixels^2. This means that the uncertainties of quantified p are large as well and thus we should not quickly draw any conclusion here. Second, we observe that all φ_f values are larger than 0.1 radian. This shows that the interactions between nanoparticles and water are very strong. Third, we observe that φ_{par} is definitely not proportional to the echo time for all four nanoparticle solutions. This means that there are other chemistry effects in those nanoparticle solutions.

As stated in the above Summary, we will need to mix nanoparticle solutions with gel for minimizing the interaction effect. By doing so, the signal-to-noise ratios (SNR) of high nanoparticle concentrations or at long echo times may become too low for reliable phase measurements. Nonetheless we will still give a try.

B. Comparisons between CISSCO, SWIM, and a QSM method from a gadolinium phantom

We submitted a manuscript to a journal about the improvement of the 2D CISSCO method that we had been working in the past few years. In that work, we filled a straw with a known concentration of gadolinium and inserted that straw in a gel phantom. We rotated and imaged the phantom with three echo times such that the straw was at three different orientations relative to the main field. We quantified the susceptibility and straw radius from the improved 2D CISSCO method for each orientation and echo time. The reviewers asked us to compare results from our CISSCO method to other quantitative susceptibility mapping (QSM) methods such as the susceptibility weighted imaging mapping (SWIM) method [Haacke et al., 2010]. As this request is consistent with some of the work statements in this grant, we made some efforts to address this question. We simulated an image with the cylindrical object perpendicular to the main field and applied CISSCO, SWIM, and the "morphology enabled dipole inversion" (MEDI) method [de Rochefort et al., 2010], which can be downloaded from http://weill.cornell.edu/mri/pages/qsm.html. Then we applied these three methods to phantom images acquired at the perpendicular orientation. In addition, we reduced the image resolution and re-quantified the susceptibility of the gadolinium straw with CISSCO. The purpose was to show that the improved 2D CISSCO method is capable for the quantifications of susceptibility and object size. From our results below, generally speaking, our CISSCO results are more accurate than SWIM and MEDI.

9

1) Methods and materials
a) Simulation

In our simulations, we assumed a susceptibility $\Delta\chi$ of 0.5 ppm and a main field of 3 T. We simulated each cylindrical object and its spin density as well as its induced magnetic field on a 4096 x 4096 matrix and converted the complex matrix to 256 x 256. We added the white noise to the 256 x 256 complex matrix. The detailed procedures of such simulations were described in [Cheng et al., 2007]. We performed most of our simulations and susceptibility quantifications on a Pentium 4 personal computer. The radius of each cylindrical object on the 256 x 256 matrix was targeted to be 1 pixel.

We simulated objects at $\theta = 90°$ and at three echo times 11, 17, and 20 ms. An effective spin density of 20 arbitrary units at TE = 0 with transverse relaxation rate, R2 = 10 s^{-1}, were used for the signals inside the cylinder at different echo times but 10 for the outside. The signal-to-noise ratio (SNR) outside the cylinder was set to 10:1. The optimal choices of radii for quantifying magnetic moments from CISSCO were described in [Cheng et al., 2009]. For the susceptibility quantification of SWIM and MEDI, we obtained the susceptibility from only one pixel inside the cylinder.

b) Important parameters of phantom studies and images

We filled a straw with 1.62 mM of the gadolinium solution and inserted that straw in a gel phantom. With the molar susceptibility of Gd-DTPA being 4π x (0.027 ± 0.001) ppm/mM [Weisskoff and Kiihne, 1992] and with the water susceptibility roughly -9.05 ppm, the estimated volume susceptibility of the gadolinium solution relative to water, $\Delta\chi$, was 0.58 ± 0.05 ppm. The diameter of the straw was 4.92 ± 0.02 mm, measured by a Vernier caliber, which led to a cross-sectional area of 19.0 ± 0.2 mm^2.

We imaged the phantom with a conventional single-echo 3D spoiled gradient echo (SPGR) sequence, in a 3 T clinical GE Discovery MR750 machine. We used a quadrature head coil for imaging. The imaging parameters were: TE = 11 ms, 17 ms, and 20 ms, TR = 30 ms, flip angle = 20°, read bandwidth = 244.14 Hz/pixel, image resolution = 1 mm x 1 mm x 1 mm, and fields of view = 256 mm x 256 mm x 28 mm. We manually changed the echo time three times to obtain images from three echoes. The acquisition time for each scan was about 4 minutes. We rotated the entire phantom including the straw and scanned the phantom in three different orientations (90°, 75.5°, and 28.2°) from the main field. We manually unwrapped phase in phase images and removed the background phase with a typical 2D quadratic fitting method. After these procedures, we referred the phase images as "cleaned" phase images. We analyzed two different slices from each orientation and each echo time to check the consistency in our phantom studies. For comparisons, we applied SWIM and MEDI only to the perpendicular orientation.

After obtaining the susceptibility maps from SWIM and MEDI (see Fig. 3c and Fig. 3d), we calculated the mean and standard deviation of the susceptibility value from four pixels completely inside the straw.
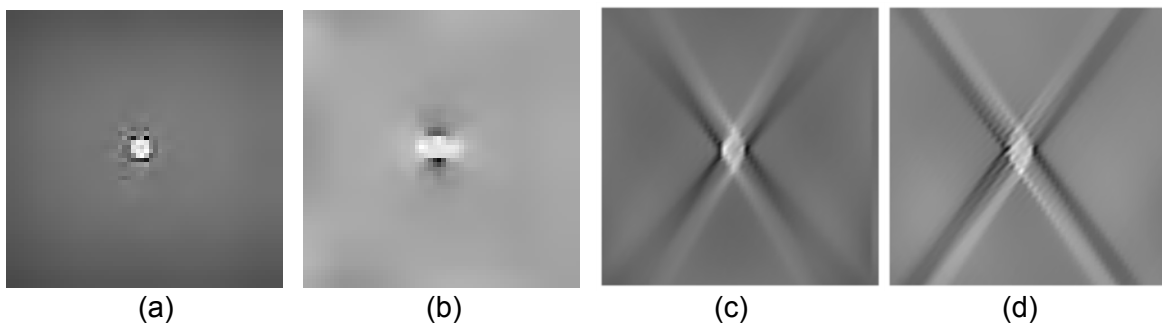

| (a) | (b) | (c) | (d) |

Figure 3: (a) The magnitude and (b) its associated cleaned phase image at TE = 20 ms were acquired from a 3T machine. The straw is shown in the middle of the magnitude image (a). Note the dipolar phase pattern around the straw in (b). (c) The corresponding susceptibility map generated from phase images using SWIM. (d) The corresponding susceptibility map generated from phase images using MEDI.

To study the effect due to different straw sizes, we reduced the image resolutions and then applied our CISSCO method for susceptibility quantifications again. For each image of interest with the original size of 256 x 256, we Fourier transformed the magnitude and cleaned phase images to k-space. Then we selected the central 128 x 128 or 100 x 100 points out of the 256 x 256 complex matrix in k-space. We inverse Fourier transformed those smaller matrices back to the image domain and obtained images with lower resolutions. As a result, the theoretical diameters of the straw became 2.46 ± 0.02 mm and 1.92 ± 0.02 mm, respectively. By doing this, we could evaluate our method in a consistent way without introducing additional experimental errors (e.g., effects due to the wall of a small straw). An example image is shown in Fig. 4.
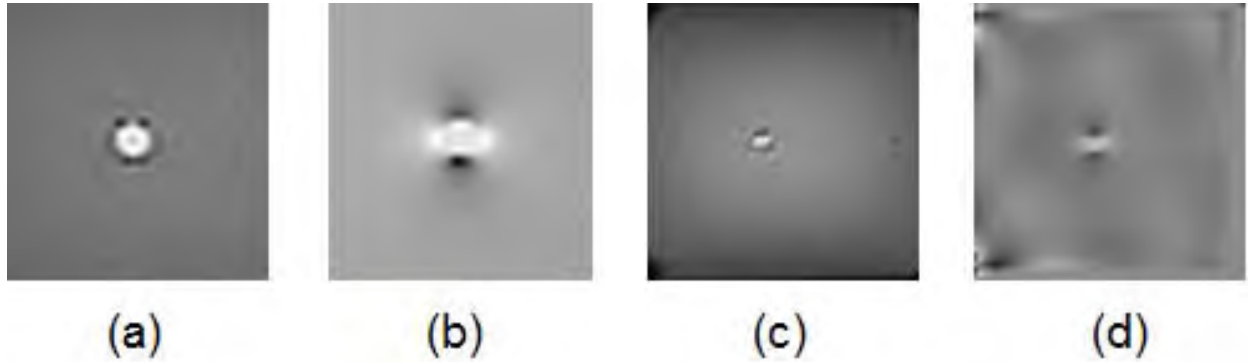

(a)   (b)   (c)   (d)

Figure 4: (a) Magnitude image of the straw at its original resolution. (b) Its associated phase image. (c) Magnitude image of the straw at a lower resolution with the 100 x 100 matrix size described in the text. (d) Its associated phase image. For the display purpose here, all four images have been cropped to 30 x 30 matrices.

2) Results
a) Simulation results

The results from simulations are shown in Table 4. As can be seen, results from our CISSCO method are accurate and close to the original input $\Delta\chi$ of 0.5 ppm. The differences between quantified susceptibilities and the actual value are no more than 8%. On the other hand, the estimated uncertainties are sometimes large due to short echo times. The results from either SWIM or MEDI are at least 25% away from the actual susceptibility value.

TE (ms)	CISSCO	SWIM[a]	MEDI[b]
11	0.54 ± 0.14	0.34	0.37
17	0.50 ± 0.03	0.24	0.65
20	0.49 ± 0.02	0.19	0.67

Comments: [a]thresholding parameter = 0.1. [b]regulation parameter = 250

Table 4: Quantified results from simulated images at three different echo times at $\theta = 90°$ using the CISSCO method, SWIM, and MEDI. The actual susceptibility value is $\Delta\chi = 0.5$ ppm. The first column lists the echo time. The second column lists the results from the CISSCO method. The third column shows the results from SWIM. The fourth column shows the results from MEDI.

b) Phantom results

Most of the measured susceptibilities from phantom studies based on our CISSCO method also agree well within 12% of the theoretical value, 0.58 ± 0.05 ppm, for all orientations, different echo times, and image resolutions. The results in 256 x 256 matrix size are listed in Tables 5, 6, and 7. The results from the 128 x 128 matrix size (lower resolution) are listed in Tables 8, 9, and 10. The results from the 100 x 100 matrix size (lowest resolution) are listed in Tables 11, 12, and 13. The measured cross-sectional areas and the theoretical value agree within 16%, except for results from the 28.2° orientation and from lower image resolutions. Some uncertainties are large due to large uncertainties propagated from quantifications of small magnetic moments.

Angle	TE	p (theory)	Slice number 12			Slice number 16		
			p	$\Delta\chi$	A	p	$\Delta\chi$	A
(degree)	(ms)	(rad·mm^2)	(rad·mm^2)	ppm	mm^2	(rad·mm^2)	ppm	mm^2
90	11	15.4	14.1 ± 0.7	0.57 ± 0.02	17.5 ± 1.1	14.5 ± 0.7	0.57 ± 0.02	18.2 ± 1.1
	17	23.9	21.9 ± 0.5	0.54 ± 0.01	19.2 ± 0.4	22.4 ± 0.4	0.55 ± 0.01	19.2 ± 0.4
	20	28.2	26.3 ± 0.5	0.54 ± 0.01	19.0 ± 0.4	26.2 ± 0.5	0.55 ± 0.01	18.7 ± 0.4

Table 5: Quantified results from phantom images of the original image resolution at three different echo times at the 90° orientation. Two different slices, 12 and 16, were analyzed. The theoretical value of $\Delta\chi$ is 0.58 ± 0.05 ppm and the actual cross-sectional area is 19.0 ± 0.2 mm^2. The SNR around and outside the straw for all three echo times is about 30:1. The SNR values inside the straw at three echo times, 11, 17, and 20 ms, are about 48:1, 44:1, and 42:1, respectively. The first column lists the orientation. The second column lists the echo time. The third column shows the theoretical magnetic moment p. The fourth and seventh columns show quantified magnetic moment p. The fifth and seventh columns list $\Delta\chi$ solved from the CISSCO method. The sixth and eighth columns show the cross-sectional area of the cylinder.

Angle	TE	p (theory)	Slice number 12			Slice number 16		
			p	$\Delta\chi$	A	p	$\Delta\chi$	A
(degree)	(ms)	(rad·mm^2)	(rad·mm^2)	ppm	mm^2	(rad·mm^2)	ppm	mm^2
75.5	11	14.5	12.9 ± 0.9	0.58 ± 0.02	16.9 ± 0.8	13.0 ± 0.9	0.60 ± 0.02	16.5 ± 0.8
	17	22.4	21.3 ± 0.4	0.54 ± 0.02	19.3 ± 0.4	21.1 ± 0.4	0.56 ± 0.02	18.6 ± 0.4
	20	26.4	24.6 ± 0.5	0.54 ± 0.01	19.0 ± 0.4	24.5 ± 0.5	0.56 ± 0.01	18.2 ± 0.4

Table 6: Quantified results from phantom images of the original image resolution at three different echo times at 75.5° orientation. The meaning of each column has been explained in Table 5.

Angle	TE	p (theory)	Slice number 12			Slice number 16		
			p	$\Delta\chi$	A	p	$\Delta\chi$	A
(degree)	(ms)	(rad·mm^2)	(rad·mm^2)	ppm	mm^2	(rad·mm^2)	ppm	mm^2
28.2	11	3.45	3.64 ± 2.87	0.60 ± 0.40	19.3 ± 12.4	3.22 ± 3.22	0.65 ± 0.44	15.8 ± 10.1
	17	5.34	6.25 ± 3.75	0.55 ± 0.12	23.4 ± 12.9	6.11 ± 3.85	0.57 ± 0.12	22.1 ± 12.1
	20	6.29	6.65 ± 3.39	0.57 ± 0.08	20.4 ± 8.2	6.97 ± 3.07	0.57 ± 0.08	21.4 ± 8.6

Table 7: Quantified results from phantom images of the original image resolution at three different echo times at 28.2° orientation. The meaning of each column has been explained in Table 5.

Angle	TE	p (theory)	Slice number 12			Slice number 16		
			p	$\Delta\chi$	A	p	$\Delta\chi$	A
(degree)	(ms)	(rad·mm^2)	(rad·mm^2)	ppm	mm^2	(rad·mm^2)	ppm	mm^2
90	11	3.85	3.30 ± 0.46	0.55 ± 0.08	4.30 ± 1.55	3.27 ± 0.46	0.57 ± 0.09	4.01 ± 1.44
	17	5.98	5.46 ± 0.44	0.51 ± 0.04	4.91 ± 0.59	5.69 ± 0.46	0.59 ± 0.04	4.45 ± 0.53
	20	7.05	6.27 ± 0.44	0.54 ± 0.03	4.52 ± 0.41	6.41 ± 0.44	0.54 ± 0.03	4.68 ± 0.42

Table 8: Quantified results from phantom images of the 128 x 128 matrix size at three different echo times at 90° orientation. The theoretical value of $\Delta\chi$ is still 0.58 ± 0.05 ppm but the cross-sectional area becomes 4.75 ± 0.05 mm^2. The SNR around and outside the straw for all three echo times is about 60:1. The SNR values inside the straw at three echo times, 11, 17, and 20 ms, are about 96:1, 88:1, and 84:1, respectively. The meaning of each column has been explained in Table 5. Two different slices, 12 and 16, were analyzed.

			Slice number 12			Slice number 16		
Angle	TE	p (theory)	p	$\Delta\chi$	A	p	$\Delta\chi$	A
(degree)	(ms)	(rad·mm^2)	(rad·mm^2)	ppm	mm^2	(rad·mm^2)	ppm	mm^2
75.5	11	3.63	3.14 ± 0.94	0.55 ± 0.13	4.30 ± 2.19	3.24 ± 0.97	0.60 ± 0.14	4.08 ± 2.08
	17	5.6	4.92 ± 0.69	0.54 ± 0.08	4.45 ± 0.62	4.94 ± 0.69	0.55 ± 0.08	4.45 ± 0.62
	20	6.6	5.79 ± 0.46	0.53 ± 0.08	4.60 ± 0.82	5.93 ± 0.47	0.55 ± 0.10	4.52 ± 0.62

Table 9: Quantified results from phantom images of the 128 x 128 matrix size at three different echo times at 75.5° orientation. The meaning of each column has been explained in Table 8.

			Slice number 12			Slice number 16		
Angle	TE	p (theory)	p	$\Delta\chi$	A	p	$\Delta\chi$	A
(degree)	(ms)	(rad·mm^2)	(rad·mm^2)	ppm	mm^2	(rad·mm^2)	ppm	mm^2
28.2	11	0.86	1.14 ± 0.97	0.46 ± 0.39	7.94 ± 10.3	1.08 ± 0.92	0.52 ± 0.44	6.61 ± 8.59
	17	1.34	1.28 ± 0.70	0.59 ± 0.25	4.45 ± 3.74	1.52 ± 0.84	0.56 ± 0.24	5.56 ± 4.67
	20	1.57	1.78 ± 0.80	0.55 ± 0.15	5.64 ± 3.61	1.83 ± 0.82	0.56 ± 0.15	5.73 ± 3.66

Table 10: Quantified results from phantom images of the 128 x 128 matrix size at three different echo times at 28.2° orientation. The meaning of each column has been explained in Table 8.

			Slice number 12			Slice number 16		
Angle	TE	p (theory)	p	$\Delta\chi$	A	p	$\Delta\chi$	A
(degree)	(ms)	(rad·mm^2)	(rad·mm^2)	ppm	mm^2	(rad·mm^2)	ppm	mm^2
90	11	2.35	1.87 ± 0.54	0.50 ± 0.25	2.66 ± 0.93	2.03 ± 0.51	0.57 ± 0.29	2.54 ± 0.89
	17	3.64	3.62 ± 0.43	0.55 ± 0.07	3.02 ± 1.06	3.52 ± 0.46	0.53 ± 0.07	3.08 ± 1.08
	20	4.3	4.23 ± 0.34	0.51 ± 0.04	3.27 ± 0.88	4.10 ± 0.37	0.53 ± 0.04	3.02 ± 0.81

Table 11: Quantified results from phantom images of the 100 x 100 matrix size at three different echo times at 90° orientation. The theoretical value of $\Delta\chi$ is still 0.58 ± 0.05 ppm but the cross-sectional area becomes 2.90 ± 0.03 mm^2. The SNR outside the straw for all three echo times is about 77:1. The SNR values inside the straw at three echo times, 11, 17, and 20 ms, are about 123:1, 113:1, and 108:1, respectively. The meaning of each column has been explained in Table 5. Two different slices, 12 and 16, were analyzed.

			Slice number 12			Slice number 16		
Angle	TE	p (theory)	p	$\Delta\chi$	A	p	$\Delta\chi$	A
(degree)	(ms)	(rad·mm^2)	(rad·mm^2)	ppm	mm^2	(rad·mm^2)	ppm	mm^2
75.5	11	2.21	1.99 ± 0.98	0.54 ± 0.22	2.78 ± 1.19	2.03 ± 0.99	0.61 ± 0.25	2.54 ± 1.09
	17	3.42	3.45 ± 1.00	0.51 ± 0.14	3.33 ± 1.47	3.20 ± 0.93	0.55 ± 0.15	2.83 ± 1.25
	20	4.03	4.01 ± 0.80	0.51 ± 0.10	3.26 ± 1.01	3.81 ± 0.76	0.55 ± 0.11	2.90 ± 0.90

Table 12: Quantified results from phantom images of the 100 x 100 matrix size at three different echo times at 75.5° orientation. The meaning of each column has been explained in Table 11.

Angle	TE	p (theory)	Slice number 12			Slice number 16		
(degree)	(ms)	(rad·mm^2)	p (rad·mm^2)	$\Delta\chi$ ppm	A mm^2	p (rad·mm^2)	$\Delta\chi$ ppm	A mm^2
28.2	11	0.53	0.57 ± 1.14	0.57 ± 1.14	3.20 ± 19.2	0.67 ± 1.34	0.58 ± 0.25	3.66 ± 22.0
	17	0.81	0.87 ± 0.77	0.57 ± 0.68	3.14 ± 5.97	0.94 ± 0.84	0.56 ± 0.67	3.46 ± 6.58
	20	0.96	1.21 ± 0.39	0.53 ± 0.15	4.01 ± 2.21	1.14 ± 0.36	0.55 ± 0.15	3.66 ± 2.02

Table 13: Quantified results from phantom images of the 100 x 100 matrix size at three different echo times at 28.2° orientation. The meaning of each column has been explained in Table 11.

For comparisons of phantom results, the susceptibility values quantified from SWIM and MEDI are listed in Table 14. All quantified values from SWIM and MEDI except for one are underestimated by at least 20% for the perpendicular orientation. For this reason, we do not quantify susceptibility values from SWIM or MEDI from other orientations or lower image resolutions, as we expect worse results for those situations. These phantom and simulated results indicate that SWIM or MEDI cannot suitably quantify susceptibility from cylindrical objects with diameters of less than 5 pixels.

Angle	TE	CISSCO		SWIM[a]		MEDI[b]	
(Degree)	(ms)	Slice 12	Slice 16	Slice 12	Slice 16	Slice 12	Slice 16
90	11	0.57 ± 0.02	0.57 ± 0.02	0.36 ± 0.02	0.36 ± 0.02	0.46 ± 0.04	0.42 ± 0.01
	17	0.54 ± 0.01	0.55 ± 0.01	0.46 ± 0.14	0.36 ± 0.08	0.47 ± 0.06	0.40 ± 0.11
	20	0.54 ± 0.01	0.55 ± 0.01	0.52 ± 0.09	0.35 ± 0.07	0.42 ± 0.09	0.40 ± 0.09
Comments: [a]thresholding parameter = 0.1. [b]regulation parameter = 250							

Table 14: Quantified magnetic susceptibilities of the same slices at 90° from Table 5, using SWIM and MEDI. For comparisons, results from our CISSCO method are listed again. The theoretical value of $\Delta\chi$ is 0.58 ± 0.05 ppm. The first column lists the orientation. The second column lists the echo time. The third and fourth columns show quantified susceptibility values from our CISSCO approach. The fifth and sixth columns show quantified susceptibility values from SWIM. The seventh and eighth columns show quantified susceptibility values from MEDI. The regulation parameters used in MEDI were suggested in their MATLAB code. Optimal choices of those regulation parameters are not known yet [Liu et al., 2012].

c) Discussion

When the orientation of a cylinder deviates from 90°, but other factors remain the same, the magnetic moment quantified from the object becomes smaller than that at 90°. As a result, the uncertainty of the magnetic moment increases and so does that of the susceptibility. In order to reduce the uncertainty, one possibility is to increase the echo time and therefore our effective magnetic moment will become larger.

Γ. Magnetic moment and susceptibility quantification of air bubbles and glass beads using 3D CISSCO

We have been improving our user friendly 3D CISSCO software since the first quarter of this grant. We apply this software to exiting phantom images published in Liu et al. [2013]. Liu et al. [2013] showed that quantified susceptibility values from SWIM on air bubbles or glass beads were much less than actual values. However, when they considered the product of the susceptibility and the effective volume within the quantified susceptibility region (i.e., the volume of interest within which a mean susceptibility value was calculated), the results were much closer to the actual values. In fact, such a product is the magnetic moment in our cases.

Here we will show that quantified magnetic moments from our 3D CISSCO are much closer to the actual magnetic moments of air bubbles. To see this, we quantify volumes of those air bubbles and calculate the susceptibility values with the volume and magnetic moment information. The susceptibility difference between the air bubble and the surrounding gel (i.e., water) is 9.4 ppm. The best answer from Liu et al. [2013] was less than 8.0 ppm even after they corrected the results with the considerations of estimated magnetic moments.

Liu et al. [2013] acquired 5-echo gradient echo and spin echo images of a gel phantom from a 2.89 T machine. We quantified magnetic moments from the gradient echo data using the 3D CISSCO and quantified volumes from the spin echo data. These are similar to our approaches to 2D cylinders (see [Cheng et al., 2009]). The phantom contained 14 air bubbles and 9 glass beads of varying sizes (diameters of 2, 3, 5, and 6 mm). Imaging parameters for the gradient echo sequence were TE = 3.93, 9.60, 15.27, 20.94, and 26.61 ms; TR = 33 ms; flip angle of 11°; read bandwidth of 465 Hz/pixel; voxel size of 0.5 mm x 0.5 mm x 0.5 mm; and matrix size of 512 x 304 x 176. Spin echo imaging was performed using the same field of views, resolution, read bandwidth, and matrix size as the gradient echo sequence; other parameters were TR = 5000 ms, TE = 15 ms, and a flip angle of 90°. We chose four air bubbles for susceptibility quantifications at either the first or second echo time due to the relative proximity between other air bubbles. We also quantified four glass beads with different sizes from the shortest echo time. We manually unwrapped phase and removed the background phase with a 3D second order polynomial fit. We show phase and magnitude images of an air bubble and glass bead in Fig. 5. As the volumes of the glass beads are known, we do not quantify those volumes from spin echo images.

(a)   (b)   (c)   (d)
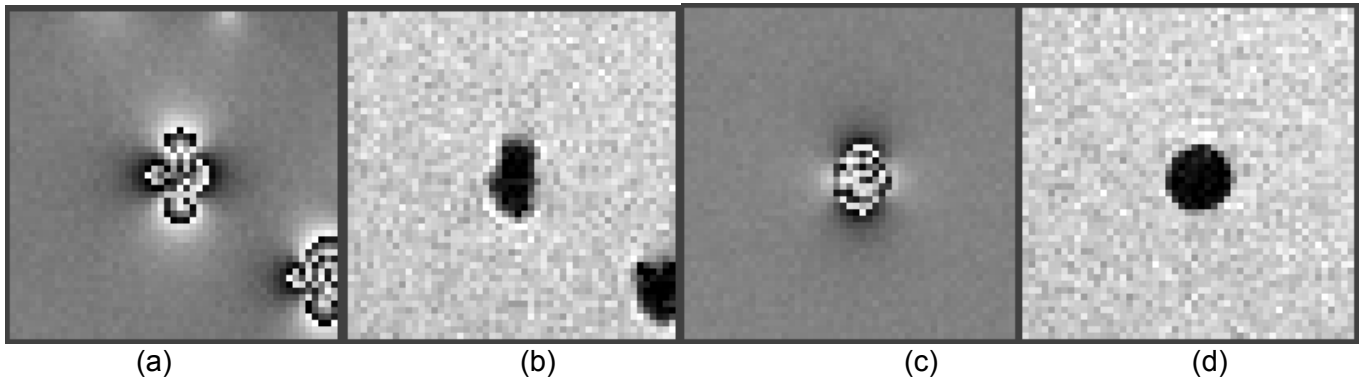
Figure 5: (a) Phase and (b) magnitude image of an air bubble in the middle of the image. (c) Phase and (d) magnitude image of a 5 mm glass bead.

Table 15 shows results of the magnetic moment, volume, susceptibility, and their theoretical uncertainties for all quantified air bubbles and glass beads. The average error in susceptibility quantification for air bubbles was 10%. This is a significant improvement over SWIM used in Liu et al. (2013). Also note that the quantified susceptibility values of air bubbles are closer to 9.4 ppm, compared to the best 8.0 ppm from Liu et al. [2013].

OBJECT	$|p|$ (radians * pixel^3)	$\delta p/p$ (%)	V (pixels^3)	$\delta V/V$ (%)	$\Delta\chi$ (ppm)	$\delta\Delta\chi/\Delta\chi$ (%)
AIR BUBBLE 1	614.34	0.01	237.40	0.88	10.31	0.88
AIR BUBBLE 2	28.80	0.10	5.40	7.41	8.70	7.41
AIR BUBBLE 3	71.76	0.07	32.88	3.56	8.70	3.56
AIR BUBBLE 4	183.32	0.02	27.50	2.33	10.87	2.33
GLASS BEAD 2 mm	21.76	0.10	33.50	0.00	2.59	0.10
GLASS BEAD 3 mm	60.87	0.04	113.10	0.00	2.14	0.04
GLASS BEAD 5 mm	242.11	0.02	523.60	0.00	1.84	0.02
GLASS BEAD 6 mm	448.51	0.01	904.78	0.00	1.98	0.01

Table 15: Results of quantified magnetic moments $|p|$, quantified volume from spin echo images (or true bead diameters) V, and calculated susceptibility $\Delta\chi$, along with their uncertainties for air bubbles and glass beads.

Results from glass beads require further investigations. This is because those results were quantified from TE = 3.93 ms. At this echo time, the phase values outside the beads are not sufficient, as we can see from Fig. 5c. For accurate magnetic moment or susceptibility quantification, we likely need a phase value of roughly π at the equatorial surface of a spherical object.

KEY RESEARCH ACCOMPLISHMENTS

The following list of key research accomplishments is based on the "Statement of Work" described in our funded grant. In this second year,

- We have re-analyzed our data and have found that the magnetic susceptibility values measured from different concentrations of ferritin and nanoparticle solutions are self consistent between echo times. When frequency shifts due to hyperfine shifts are corrected, the susceptibility values quantified from CISSCO agree with values measured from phase inside objects (straws). Using the phase distributions outside those straws, CISSCO has quantified the actual magnetic moment in each case.
- We have demonstrated from simulations and phantom studies that our CISSCO method is more accurate in susceptibility quantifications than other current (and popular) methods such as SWIM or MEDI. This is especially the case when an object of interest is no more than 5 pixels in size.
- We have applied the CISSCO method for the susceptibility quantifications of air bubbles and glass beads. The results again are more accurate than those from SWIM.

REPORTABLE OUTCOMES

Manuscripts, abstracts, or presentations with partial supports from this grant:

- S. Liu, K. Mok, J. Neelavalli, Y.-C. N. Cheng, J. Tang, Y. Ye, and E. M. Haacke, *Improved MR venography using quantitative susceptibility-weighted imaging*, Journal of Magnetic Resonance Imaging, vol. 40, no. 3, pp. 698-708, 2014. (attached at the end of this report)
- S. Buch, S. Liu, Y. Ye, Y.-C. N. Cheng, J. Neelavalli, and E. M. Haacke, *Susceptibility mapping of air, bone, and calcium in the head*, Magnetic Resonance in Medicine, in press.
- C.-Y. Hsieh, Y.-C. N. Cheng, J. Neelavalli, E. M. Haacke, and R. J. Stafford, An improved method for susceptibility and radius quantification of cylindrical objects from MRI, submitted to Magnetic Resonance Imaging for review.
- *Quantitative Susceptibility Mapping*, a talk presented by E. M. Haacke at Workshop on Standards for Quantitative MRI, National Institute of Standards and Technology (NIST), Boulder, Colorado, USA, July 14, 2014.
- *Magnetic susceptibility in MRI,* a talk presented by Y.-C. N. Cheng at the Third QSM Workshop, Duke University, Durham, North Carolina, USA, October 6, 2014.

Funding applied for based on work supported by this award:

- DOD/CDMRP/PRARP, Title: Quantifying absolute magnetic moments and susceptibilities of tissues and microbleeds as an MRI tool for diagnosing AD at an early stage derived from TBI.

Employment or research opportunities applied for and/or received based on experience/training supported by this award:

- None.

CONCLUSION

In this second year, due to the disruption of funding which led to the suspension of our research for the majority of this year, we have made limited progress. However, we have spent time to carefully re-analyze our data and have tried to understand the details of certain scientific problems. We continue to accomplish tasks outlined in the Statement of Work. The above list of key accomplishments serves as a summary of the conclusion. In brief, our CISSCO method can accurately quantify the magnetic moment of a relatively small object. When the volume of the object is known, we can calculate the magnetic susceptibility. The accuracy

achieved by CISSCO on an object with a diameter of a few pixels cannot be achieved by any other current susceptibility quantification methods. We have now shown no inconsistencies between susceptibility values quantified from phase values inside objects (straws) and susceptibilities estimated from phase values outside straws using CISSCO. The key point is to determine the additional frequency shifts inside objects due to hyperfine shifts or chemical interactions. This will be important for the MR community to be aware. We will also need to spend time to write and publish our above work.

In the next annual period, as listed in the Statement of Work, we will use or build molds to prepare samples with arbitrary geometries and quantify the susceptibility of each sample. We will also need to improve our own background phase removal method to a 3D method. In addition to existing susceptibility quantification methods, we also want to develop a better method or continue to improve all those methods. These will be challenging tasks in this coming annual period.

REFERENCES

Y.-C. N. Cheng, C.-Y. Hsieh, J. Neelavalli, Q. Liu, M. S. Dawood, and E. M. Haacke, *A complex sum method of quantifying susceptibilities in cylindrical objects: The first step toward quantitative diagnosis of small objects in MRI*, Magnetic Resonance Imaging, 25(8): 1171-1180, 2007.

Y.-C. N. Cheng, C.-Y. Hsieh, J. Neelavalli, and E. M. Haacke, *Quantifying effective magnetic moments of narrow cylindrical objects in MRI*, Physics in Medicine and Biology, 54: 7025-7044, 2009.

S. C.-K. Chu, Y. Xu, J. Balschi, and C. Springer, *Bulk magnetic susceptibility shifts in NMR studies of compartmentalized samples: Use of paramagnetic reagents*, Magnetic Resonance in Medicine, 13: 239-262, 1990.

S. Fossheim, C. Johansson, A. K. Fahlvik, D. Grace, and J. Klaveness, *Lanthanide-based susceptibility contrast agents: assessment of the magnetic properties*, Magnetic Resonance in Medicine, 35: 201-206, 1996.

E. M. Haacke, J. Tang, J. Neelavalli, and Y.-C. N. Cheng, *Susceptibility mapping as a means to visualize veins and quantify oxygen saturation*, Journal of Magnetic Resonance Imaging, 32: 663-676, 2010.

T. Liu, W. Xu, P. Spincemaille, A. Avestimehr, and Y. Wang, *Accuracy of the morphology enabled dipole inversion (MEDI) algorithm for quantitative susceptibility mapping in MRI*, IEEE Transactions on Medical Imaging 31(3): 816-824, 2012.

S. Liu, J. Neelavalli, Y.C.N. Cheng, J. Tang, and E. M. Haacke, Quantitative susceptibility mapping of small objects using volume constraints, Magnetic Resonance in Medicine, 69: 716-723, 2013.

L. de Rochefort, T. Liu, B. Kressler, J. Liu, P. Spincemaille, V. Lebon, J. Wu, and Y. Wang, *Quantitative susceptibility map reconstruction from MR phase data using Bayesian regularization: Validation and application to brain imaging*, Magnetic Resonance in Medicine 63(1): 194-206, 2010.

F. Schweser, A. Deistung, B. W. Lehr, and J. R. Reichenbach, *Quantitative imaging of intrinsic magnetic tissue properties using MRI signal phase: An approach to in vivo brain iron metabolism?*, NeuroImage, 54: 2789-2807, 2011.

R. M. Weisskoff and S. Kiihne, *MRI susceptometry: image-based measurement of absolute susceptibility of MR contrast agent and human blood*, Magnetic Resonance in Medicine, 24: 375-383, 1992.

APPENDICES

The paper by Liu et al. is attached.

Original Research

Improved MR Venography Using Quantitative Susceptibility-Weighted Imaging

Saifeng Liu, BS,[1] Karen Mok, MS,[1] Jaladhar Neelavalli, PhD,[2]* Yu-Chung N. Cheng, PhD,[2] Jin Tang, PhD,[3] Yongquan Ye, PhD,[2] and E. Mark Haacke, PhD[1,2,3]

Purpose: To remove the geometry dependence of phase-based susceptibility weighting masks in susceptibility-weighted imaging (SWI) and to improve the visualization of the veins and microbleeds.

Materials and Methods: True SWI (tSWI) was generated using susceptibility-based masks. Simulations were used to evaluate the influence of the characteristic parameters defining the mask. In vivo data from three healthy adult human volunteers were used to compare the contrast-to-noise-ratios (CNRs) of the right septal vein and the left internal cerebral vein as measured from both tSWI and SWI data. A traumatic brain injury (TBI) patient dataset was used to illustrate qualitatively the proper visualization of microbleeds using tSWI.

Results: Compared with conventional SWI, tSWI improved the CNR of the two selected veins by a factor of greater than three for datasets with isotropic resolution and greater than 30% for datasets with anisotropic resolution. Veins with different orientations can be properly enhanced in tSWI. Furthermore, the blooming artifact due to the strong dipolar phase of microbleeds in conventional SWI was reduced in tSWI for the TBI case.

Conclusion: The use of tSWI overcomes the geometric limitations of using phase and provides better visualization of the venous system, especially for data collected with isotropic resolution.

SUSCEPTIBILITY-WEIGHTED IMAGING (SWI) is a high-resolution, spoiled gradient echo (GRE) magnetic resonance imaging (MRI) technique used today clinically for evaluating small veins and venous abnormalities in the brain and the presence of increased iron content and microbleeds in diseases such as dementia, multiple sclerosis, Parkinson's disease, stroke, and traumatic brain injury (1–3). SWI's exquisite sensitivity to small tissue magnetic susceptibility changes is due to its use of phase information (3–5). Paramagnetic or diamagnetic substances relative to water such as blood products or calcium, respectively, perturb the local magnetic field proportional to their respective magnetic susceptibilities. These differences are reflected in the phase of the MR images. In conventional SWI, after applying appropriate unwrapping and/or filtering techniques on the raw phase data (1,3), a phase-dependent mask is created and multiplied n times into the magnitude data to enhance the contrast/visibility of these substances.

Although SWI has been used quite successfully in clinical applications for many years, it is important to realize that it has a few weaknesses. One of them is based on the fact that the MRI phase signal is not only a function of the susceptibility, but also dependent on shape and orientation of the structure of interest. In data acquired with sufficient resolution, the phase inside veins perpendicular to the field has the opposite sign to that inside veins parallel to B_0. This leads to variable suppression effects with the phase mask that makes SWI unique over conventional gradient echo imaging (6). Recently, quantitative susceptibility mapping (QSM) has emerged as a means to extract the source of phase information, that is, the local susceptibility distribution (7–15). QSM is known to be independent of echo time and, to a large degree, of orientation. To avoid the vessel orientation dependence in routine SWI data, instead of phase we propose using a mask based on the susceptibility map. We

[1]School of Biomedical Engineering, McMaster University, Hamilton, Ontario, Canada.

[2]Department of Radiology, Wayne State University, Detroit, Michigan, USA.

[3]MRI Institute for Biomedical Research, Detroit, Michigan, USA.

*Address reprint requests to: J.N., HUH-MR Research G030/ Radiology, 3990 John R St., Detroit, MI 48201.
E-mail: jaladhar@wayne.edu

refer to this approach as true-SWI (tSWI) to distinguish it from the conventional phase mask-based SWI. In this work, our purpose is to compare the ability of these two methods to improve venous contrast and to show that tSWI is able to remove the geometry dependence of the phase for veins and microbleeds in SWI data.

MATERIALS AND METHODS

To provide some flexibility in generating the susceptibility weighting mask, W, we introduce both lower and upper thresholds for defining the mask as follows:

$$W = \begin{cases} 1 & \text{for } \chi \leq \chi_1 \\ 1 - \dfrac{\chi - \chi_1}{\chi_2 - \chi_1} & \text{for } \chi_1 < \chi \leq \chi_2 \\ 0 & \text{for } \chi > \chi_2 \end{cases} \quad [1]$$

where χ refers to the susceptibility value of a voxel (e.g., vein) relative to the surrounding tissue in the susceptibility map, χ_1 is the lower limit and χ_2 is the upper limit of the range of tissue susceptibility values for which we want to improve the contrast in the final SWI. Finally, the tSWI is generated by multiplying the magnitude image with the mask n times similar to the usual SWI mask application:

$$tSWI = mag \cdot W^n \quad [2]$$

In order to determine appropriate values for these two thresholds, we examined different potential choices. For χ_1, we used: 1) the mean susceptibility value in the background white matter tissue region (0 ppm) in the susceptibility map, and 2) three standard deviations ($3\sigma_\chi$) above the tissue region, where σ_χ is the standard deviation of the white matter tissue region in the susceptibility map. While a threshold of 0 ppm would ensure that the susceptibility weighting mask would include smaller veins that are partial volumed, it can also lead to increased noise in tissue regions where susceptibility is supposed to be zero. On the other hand, a choice of $\chi_1 = 3\sigma_\chi$ would reduce inclusion of noise in the mask. For χ_2 we used: 1) the expected mean susceptibility value in the vein, which is about 0.45

ppm relative to water (3,16) under normal physiological conditions; and 2) a value higher than this, in this case 1 ppm. For a given set of χ_1 and χ_2 values, the contrast-to-noise ratio (CNR) between the vein and the background tissue can be optimized by choosing an appropriate n value in Eq. (2). CNR for a vein can be defined as the ratio between tSWI signal contrast for the vein and its associated uncertainty as follows:

$$CNR = \frac{|S_{ref,tSWI} - S_{vein,tSWI}|}{\sigma_t} \quad [3]$$

where $\sigma_t = \sqrt{\sigma_{ref,tSWI}^2 + \sigma_{vein,tSWI}^2}$. Noise in either the reference (background tissue) region ($\sigma_{ref,\ tSWI}$) or in the vein ($\sigma_{vein,tSWI}$) in the tSWI image can be estimated using the following equation:

$$\sigma_{tSWI} = \sqrt{W^{2n}\sigma_{mag}^2 + mag^2 n^2 W^{2n-2}\sigma_W^2} \quad [4]$$

The noise, represented by the standard deviation for a given voxel in W, σ_W, is dependent on the noise, σ_χ, in the susceptibility map in the following manner:

$$\sigma_W = \begin{cases} \dfrac{\sigma_\chi}{\chi_2 - \chi_1} & \text{for } \chi_1 < \chi < \chi_2 \\ 0 & \text{for } \chi < \chi_1 \text{ or } \chi > \chi_2 \\ \dfrac{\sigma_\chi}{2(\chi_2 - \chi_1)} & \text{for } \chi = \chi_1 \text{ or } \chi = \chi_2 \end{cases} \quad [5]$$

The factor $1/2$ in the case when $\chi = \chi_1$ or $\chi = \chi_2$ in Eq. (5) is due to the discontinuity (1).

For simplicity, we assume that signal from vein (or cylinder) and reference region in the original magnitude images are the same: $mag_{ref} = mag_{vein} = S$, and their associated signal standard deviations in these two regions are also the same: $\sigma_{ref,mag} = \sigma_{vein,mag} = \sigma$. Furthermore, we assume that the mean susceptibility value of the reference region is 0, and the mean susceptibility value of the vein is χ_v.

i) When a threshold of $\chi_1 = 0$ was used to generate the susceptibility mask, in the reference region, $W = 1$, and $\sigma_W = \sigma_\chi/(2\chi_2)$. In the vein, $W = 1 - \chi_v/\chi_2$, $\sigma_W = \sigma_\chi/\chi_2$, for $\chi_1 < \chi_v < \chi_2$; but when $\chi_v = \chi_2$, $W = 0$, $\sigma_W = \sigma_\chi/(2\chi_2)$; when $\chi_v > \chi_2$, $W = 0$, $\sigma_W = 0$. Using Eq. (4):

$$\sigma_t = \begin{cases} \left(\sigma^2 + \dfrac{S^2 n^2 \sigma_\chi^2}{4\chi_2^2} + \sigma^2 \left(1 - \dfrac{\chi_v}{\chi_2}\right)^{2n} + S^2 n^2 \left(1 - \dfrac{\chi_v}{\chi_2}\right)^{2n-2} \dfrac{\sigma_\chi^2}{\chi_2^2} \right)^{1/2} & \text{for } \chi_1 < \chi_v < \chi_2 \\[4mm] \left(\sigma^2 + \dfrac{S^2 \sigma_\chi^2}{4\chi_2^2} + \dfrac{S^2 \sigma_\chi^2}{4\chi_2^2} \right)^{1/2} & \text{for } \chi_v = \chi_2, n = 1 \\[4mm] \left(\sigma^2 + \dfrac{S^2 n^2 \sigma_\chi^2}{4\chi_2^2} \right)^{1/2} & \text{for } \chi_v = \chi_2, n > 1; or \ \chi_v > \chi_2 \end{cases} \quad [6]$$

ii) When a threshold of $\chi_1 = 3\sigma_\chi$ was chosen, in the reference region, $W = 1$, and $\sigma_W = 0$ due to the fact that most pixels in the reference (background tissue) region have susceptibility values less than $3\sigma_\chi$.

In the vein, $W = 1 - (\chi_v - 3\sigma_\chi)/(\chi_2 - 3\sigma_\chi)$, $\sigma_W = \sigma_x/(\chi_2 - 3\sigma_\chi)$, for $\chi_1 < \chi_v < \chi_2$; but when $\chi_v = \chi_2$, $W = 0$, $\sigma_W = \sigma_\chi/2(\chi_2 - 3\sigma_\chi)$; when $\chi_v > \chi_2$, $W = 0$, $\sigma_W = 0$. Thus,

$$\sigma_t = \begin{cases} \left(\sigma^2 + \sigma^2\left(1 - \dfrac{\chi_v - 3\sigma_\chi}{\chi_2 - 3\sigma_\chi}\right)^{2n} + S^2 n^2\left(1 - \dfrac{\chi_v - 3\sigma_\chi}{\chi_2 - 3\sigma_\chi}\right)^{2n-2}\dfrac{\sigma_\chi^2}{(\chi_2 - 3\sigma_\chi)^2}\right)^{1/2}, & \text{for } \chi_1 < \chi_v < \chi_2 \\[2ex] \left(\sigma^2 + S^2 n^2\dfrac{\sigma_\chi^2}{4(\chi_2 - 3\sigma_\chi)^2}\right)^{\frac{1}{2}}, & \text{for } \chi_v = \chi_2, n = 1 \\[2ex] \sigma, & \text{for } \chi_v = \chi_2, n > 1; or\, \chi_v > \chi_2 \end{cases} \quad [7]$$

Thus, the CNR can be written as:

$$CNR = S\left(1 - \left(1 - \frac{\chi_v - \chi_1}{\chi_2 - \chi_1}\right)^n\right)\Big/\sigma_t \quad [8]$$

for $\chi_1 < \chi_v \le \chi_2$, with σ_t given in Eqs. (6) and (7).

When $\chi_1 = 3\sigma_\chi$ and χ_v is slightly less than χ_2, CNR approaches signal-to-noise ratio (SNR) in the magnitude images as n approaches infinity. In this case, the optimal n was chosen to be the value where CNR reaches 90% of the maximal CNR for a certain vein.

Simulations

To evaluate the theoretical predictions, the optimal choice of n for generating tSWI images for different threshold values and vessel susceptibility values, and the influence of highpass filtering on the final CNR for veins in tSWI images, simulations were performed using cylinders as surrogates to veins. A series of cylinders with radii ranging from 2 pixels to 16 pixels was used to simulate the associated phase images in a 512×512 matrix at $B_0 = 3$T, and TE = 10 msec. The cylinders were taken to be perpendicular to the main magnetic field. The input susceptibility of the cylinders was set to be 0.45 ppm and the susceptibility value of the background region was set to zero. In order to simulate a more realistic response of the field perturbation, the complex data of a cylinder with radius 16 times of the final radius was first created on an 8192×8192 matrix. The magnitude signal for the cylinder and background region were taken to be unity. The central 512×512 k-space points generated from the larger matrix were then used to reconstruct the complex images of the cylinders. Gaussian noise was added to both real and imaginary channels of the data to simulate the SNR in the magnitude images to be 10:1. The simulated phase images were processed using a homodyne highpass filter with a k-space window size of 64×64. Two sets of susceptibility maps, one from unfiltered and the other from filtered phase images, were generated for each cylinder size, using truncated k-space division with a k-space threshold of 0.1 (7). This is to evaluate the influence of highpass filtering on the final CNR in tSWI images. The tSWI images were generated using Eqs. (1) and (2) for different values of χ_1 and χ_2 as mentioned in the previous section. The standard deviation of the susceptibility maps was measured from a reference region outside the cylinder. The susceptibility mask was multiplied into the magnitude image n times with n ranging from 0 to 10 ($n = 0$ refers to the case of no

mask multiplication). The local CNRs between cylinders and the background reference were measured from the tSWI data using:

$$CNR_{measured} = |S_{vein} - S_{ref}|/\sigma_t \quad [9]$$

where S_{vein} and S_{ref} are the mean intensity values inside the cylinder (vein) and inside a reference region of interest (ROI) adjacent to the cylinder directly from the tSWI image, respectively. In order to estimate the overall noise σ_t directly from tSWI images, the standard deviations inside the cylinder ($\sigma_{vein,tSWI}$) and the reference region ($\sigma_{ref,tSWI}$) in tSWI were measured and σ_t was again calculated as the square root of $\sigma_{vein,tSWI}^2 + \sigma_{ref,tSWI}^2$. The theoretically predicted CNRs from Eq. (8) using different thresholds for generating the susceptibility mask were compared with those measured from the simulations and the appropriate value for χ_2 for processing in vivo data was determined. CNRs of the cylinders with different susceptibility values ranging from 0.2 ppm to 0.45 ppm were calculated to evaluate the influence of the susceptibility value of the object on the optimal choice of n.

In Vivo Data

To evaluate the efficacy of tSWI in in vivo neuroimaging, we compared the CNR obtained in tSWI data with that obtained in conventional SWI images in three healthy adult volunteers. The study was approved by the local Institutional Review Board and informed consent was obtained from all subjects before the MRI scan. The volunteers were imaged on a 3T Verio system (Siemens, Erlangen, Germany) using a 3D SWI sequence with isotropic voxel size of $0.5 \times 0.5 \times 0.5$ mm^3. Imaging parameters are given in Table 1. Data were acquired in the transverse orientation. In one case (volunteer 1), the SWI sequence was performed twice using two different echo times (TE = 14.3 msec and 17.3 msec). To evaluate the influence of voxel aspect ratio on the CNR, lower resolution images of $0.5 \times 0.5 \times 2$ mm^3 (anisotropic voxel size) from all four volunteer datasets were generated by taking the central portion of the original k-space along the transverse direction.

The quantitative susceptibility maps were generated for the isotropic and the anisotropic data as follows: tissues outside the brain were removed using the Brain Extraction Tool (BET) in FSL (17), a homodyne highpass filter with a k-space window of 64×64 was applied to remove the background field induced phase artifacts (1), and the inversion process to create susceptibility maps was accomplished using a single

Table 1
Imaging Parameters for Three Volunteers and One Patient For In Vivo Studies

Dataset no.	1	2	3	4	5
Volunteer no.	1	1	2	3	—
B_0 (T)	3	3	3	3	3
TR (msec)	26	26	24	24	29
TE (msec)	14.3	17.3	17	15.3	20
FA (degrees)	15	15	15	12	15
BW (Hz/px)	121	121	181	121	120
Voxel size (mm^3)	0.5x0.5x0.5	0.5x0.5x0.5	0.5x0.5x0.5	0.5x0.5x0.5	0.5x0.5x2
Matrix size	512x368x256	512x368x256	512x368x224	512x368x192	512x416x64

Dataset 5 was collected on a TBI patient.

orientation truncated *k*-space division approach with a *k*-space truncation threshold of 0.1 (7). Similar to the case of the simulated data, two sets of tSWI images for each of the SWI datasets were generated using Eqs. (1) and (2) with: a) $\chi_1 = 0$ and b) $\chi_1 = 3\sigma_\chi$, where σ_χ is the standard deviation of the susceptibility in the background white matter region close to the vein for which the CNR was measured. The threshold χ_2 was kept at 0.45 ppm. The susceptibility mask was multiplied into the magnitude image *n* times, with *n* ranging from 1 to 10. To generate conventional SWI images, phase masks were created using the highpass filtered phase images and then multiplied four times into the magnitude images (1). To investigate the impact of newer data processing methods, we also applied phase unwrapping (18) and SHARP (9) to remove the background field, and applied a geometry constrained iterative algorithm (8) to reconstruct the susceptibility maps for one dataset (Dataset 2). Then, tSWI images were generated using $\chi_1 = 0$ and $\chi_2 = 0.45$ ppm. Local CNRs of two selected veins, the left internal cerebral vein (LICV) and the right septal vein

(RSV), were measured from both tSWI and SWI using Eq. (9). Each vessel's ROI was selected from the susceptibility maps and copied onto the tSWI or SWI images for CNR evaluation. The reference ROI adjacent to each vein was taken from the same slice. To demonstrate the advantages of using tSWI over conventional SWI, we also analyzed one SWI dataset from a TBI patient. For this patient dataset, susceptibility maps were generated through homodyne highpass filtering and truncated *k*-space division. tSWI images were then obtained with susceptibility weighting masks generated using $\chi_1 = 0$, $\chi_2 = 0.45$ ppm and $n = 2$. All the processing was done using MatLab (R2010a, MathWorks, Natick, MA).

RESULTS

Simulations

The simulated phase images of cylinders of different sizes, their corresponding susceptibility maps, and tSWI images are shown in Fig. 1. The measured CNRs
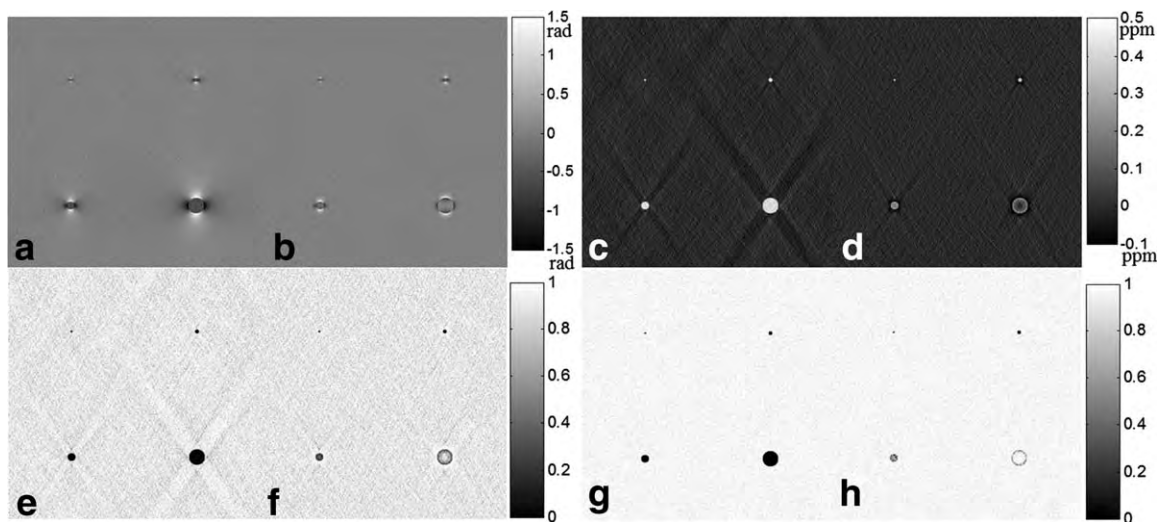

Figure 1. Phase images (**a,b**), susceptibility maps (**c,d**) and tSWI images (**e–h**) for simulated cylinders with and without homodyne highpass filtering. Images in the first and third columns are generated using the original phase images without highpass filtering, while images in the second and fourth columns are generated using highpass filtering. The tSWI images **e,f** were generated using $\chi_1 = 0$, $\chi_2 = 0.45$ ppm, $n = 2$; while **g,h** were generated using $\chi_1 = 3\sigma_\chi$, $\chi_2 = 0.45$ ppm, $n = 4$. σ_χ is the standard deviation of a reference region measured from the susceptibility maps shown in c,d ($\sigma_\chi = 0.05$ ppm for both **c,d**). The SNR in the original magnitude image was set to 10:1 and the CNR between the cylinders and background in the original magnitude images was basically zero.
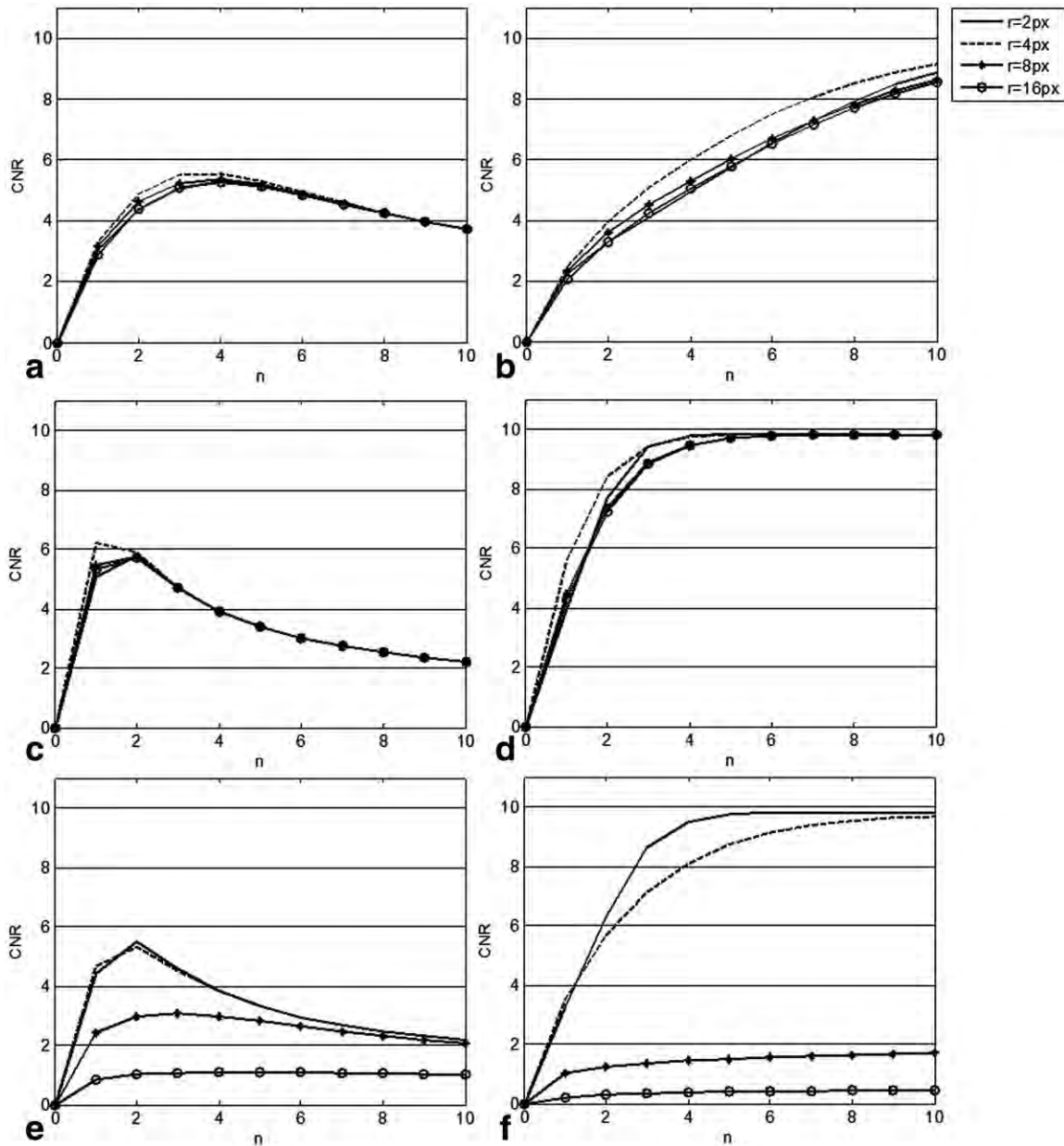
Figure 2. Measured CNRs of cylinders from simulated tSWI images. Figures in different rows were generated using different χ_2 values, while figures in different columns were generated using different χ_1 values. **(a)** $\chi_1 = 0$, $\chi_2 = 1$ ppm; **(b)** $\chi_1 = 3\sigma_\chi$, $\chi_2 = 1$ ppm; **(c)** $\chi_1 = 0$, $\chi_2 = 0.45$ ppm; **(d)** $\chi_1 = 3\sigma_\chi$, $\chi_2 = 0.45$ ppm; **(e)** $\chi_1 = 0$, $\chi_2 = 0.45$ ppm; and **(f)** $\chi_1 = 3\sigma_\chi$, $\chi_2 = 0.45$ ppm. To evaluate the effect of highpass filtering, e,f were generated using highpass filtered phase images.

for cylinders with different radii, but with a constant input susceptibility of 0.45 ppm, are plotted as a function of n in Fig. 2, and the theoretically predicted CNRs are plotted in Fig. 3. Since no T2* effects are considered here, the CNRs shown in Figs. 2 and 3 reflect contrasts from only phase/susceptibility differences between the cylinders and the background reference region. The optimal choice of n and, correspondingly, the value of CNR in the tSWI image, are influenced both by a) the choices of χ_1 and χ_2 and b) the highpass filter. For $\chi_1 = 0$, CNRs reach maximum when $n \leq 4$ (Figs. 2a,c,e, 3a,c). When χ_2 is larger with $\chi_1 = 0$, it also takes a larger n value to reach the optimized CNR. Meanwhile, the choices of χ_1 and χ_2 can also affect the rate at which optimal CNR is

approached as a function of n. For $\chi_1 = 3\sigma_\chi$, CNRs in general increase as n increases (Figs. 2b,d,f, 3b,d). The optimal n may be chosen when CNR reaches 90% of the maximum of CNR. The optimal n was 4 for $\chi_2 = 0.45$ ppm, and greater than 10 for $\chi_2 = 1$ ppm.

When a highpass filtered phase was used, the optimal choice of n was not affected much for $\chi_1 = 0$ and $\chi_2 = 0.45$ ppm (Fig. 2e), but was slightly bigger for $\chi_1 = 3\sigma_\chi$, and $\chi_2 = 0.45$ ppm for all the cylinders except for the smallest one (Fig. 2f). For both $\chi_1 = 0$ and $\chi_1 = 3\sigma_\chi$, the maximal CNR was reduced for bigger cylinders, when the highpass filter was used. This is also partly evident in Fig. 1. The behavior in the case when the highpass filtered phase was used agreed with the pattern observed in the theoretically predicted CNRs
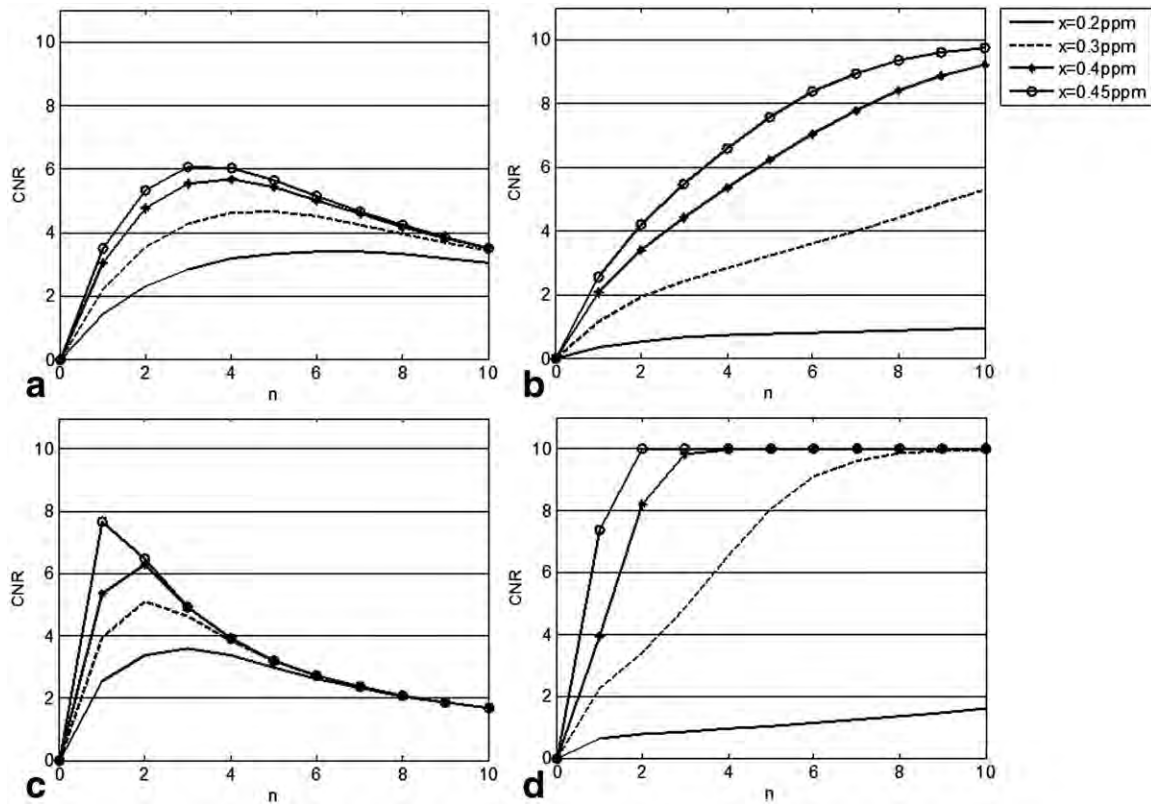
Figure 3. Theoretically predicted CNRs of cylinders with different susceptibility values. Figures in different rows were generated using different χ_2 values, while figures in different columns were generated using different χ_1 values. **(a)** $\chi_1 = 0$, $\chi_2 = 1$ ppm; **(b)** $\chi_1 = 3\sigma_\chi$, $\chi_2 = 1$ ppm; **(c)** $\chi_1 = 0$, $\chi_2 = 0.45$ ppm; and **(d)** $\chi_1 = 3\sigma_\chi$, $\chi_2 = 0.45$ ppm.

for objects with low susceptibility in Fig. 3. Given the simulated results shown in Fig. 2, we chose $\chi_2 = 0.45$ ppm in the in vivo studies for a consistent choice of n for the maximal CNR.

In Vivo tSWI

The local CNRs of the two veins, 1) the right septal vein and 2) the left internal cerebral vein, normalized by the SNRs, are plotted in Figs. 4 and 5 for all the in vivo datasets. The normalized CNRs in the SWI images and in the original magnitude images, as well as the SNRs in the original magnitude images (from the background tissues) are shown in Table 2. Compared to the original magnitude images, SWI improves the local CNR of the right septal vein in the anisotropic data, but not in the isotropic data. The CNR of the left internal cerebral vein is not improved in SWI in either isotropic or anisotropic data, due to the amplification of the noise in the background tissue region. Compared with the CNRs in magnitude images, the local CNRs in tSWI were improved by roughly a factor of 2 in both isotropic and anisotropic cases for $\chi_1 = 0$. Compared with conventional SWI, the CNRs were improved by a factor of greater than three for datasets with isotropic resolution and greater than 30% for datasets with anisotropic resolution in tSWI. The local CNRs were further improved when $\chi_1 = 3\sigma_\chi$. Considering all cases, when $\chi_1 = 0$ was used, $n = 2$ was a reasonable practical choice for both isotropic and anisotropic datasets; when $\chi_1 =$

$3\sigma_\chi$ was used, $n = 4$ was a reasonable choice for isotropic datasets and $n = 8$ for anisotropic datasets. When SHARP along with an iterative algorithm (8) was used to generate susceptibility maps, the CNRs of the two veins of interest in the corresponding tSWI image were improved, as shown in Figs. 4c,d, 5c,d. For isotropic resolution, at $n = 2$ with $\chi_1 = 0$, the relative improvements for the left internal cerebral vein and the right septal vein were 23% and 14%, respectively. For anisotropic resolution and at $n = 2$, the relative improvements for the two veins were less than 5%. However, this improvement in CNR was more significant for gray matter structures than for veins, as can be seen from Fig. 6d,h.

In Fig. 6, we compare the tSWI and SWI minimum intensity projections for both the isotropic and anisotropic cases. The tSWI appears to have higher CNR than the conventional SWI in both isotropic and anisotropic data. For tSWI, isotropic data provided a better delineation of the venous structures, compared to the anisotropic data. This is consistent with the results shown in Figs. 4 and 5, in which the normalized maximal CNRs are higher for the isotropic data than those for the anisotropic data. When $\chi_1 = 3\sigma_\chi$ was used, the visibility of some tiny veins and the gray matter structures was reduced compared to the case when $\chi_1 = 0$ was used.

As an example of this process with $\chi_1 = 0$, $\chi_2 = 0.45$ ppm and $n = 2$, Fig. 7 shows a case that demonstrates the problems with the conventional SWI processing: one of the veins has a trajectory roughly at the
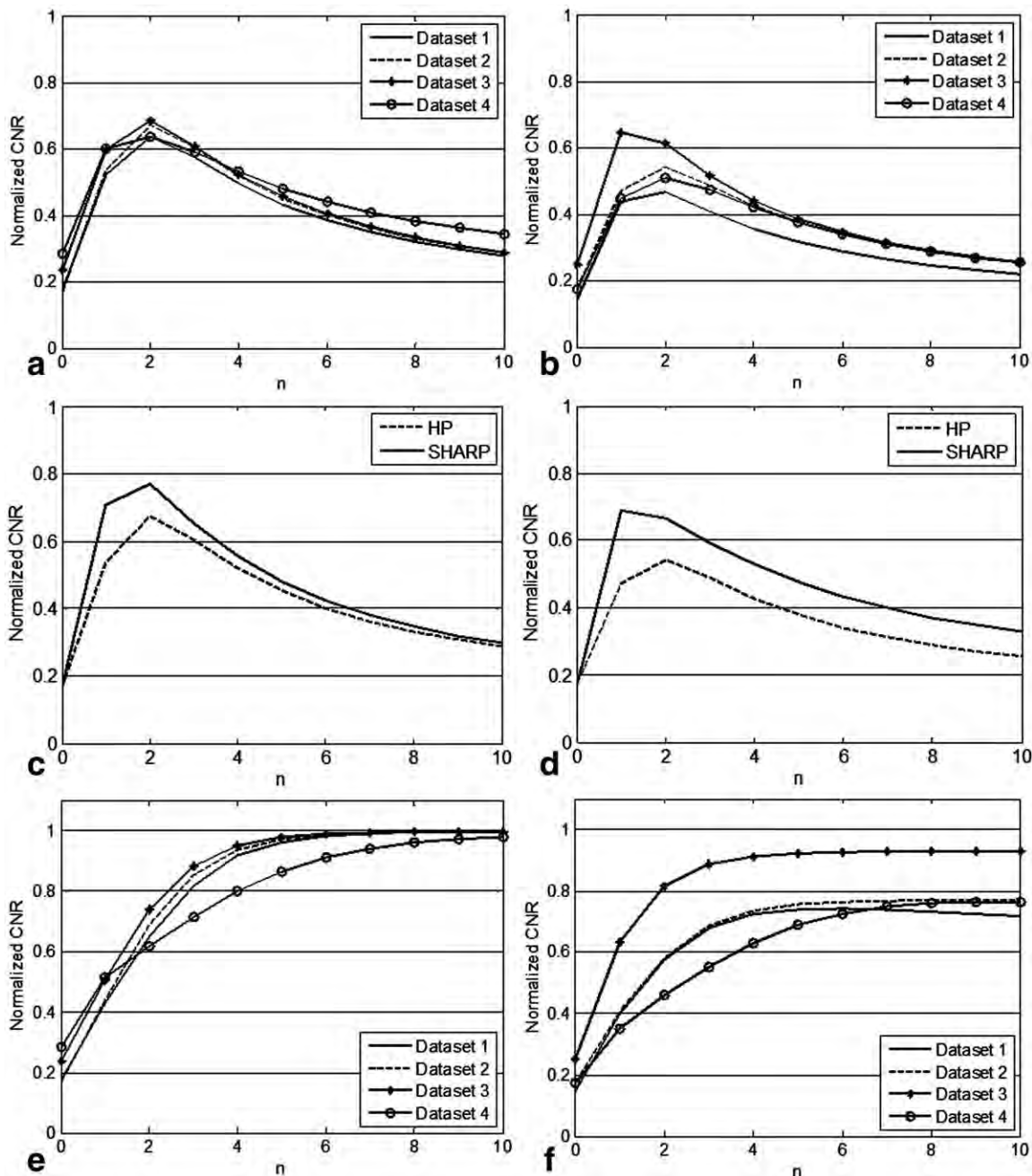
Figure 4. Local CNRs of the right septal vein (**a,c,e**) and the left internal cerebral vein (**b,d,f**) from different datasets with isotropic resolution. **a–d**: Generated when threshold $\chi_1 = 0$ was used to create the susceptibility weighting masks, while **e,f** were generated when $\chi_1 = 3\sigma_\chi$ was used. The CNRs were normalized by the corresponding SNRs listed in Table 2. **c,d**: The CNRs of the two veins in Dataset 2 with isotropic resolution, when different data processing methods were used for susceptibility mapping (see Fig. 6 for examples of the tSWI images).

magic angle (54.7°) with respect to the direction of the main magnetic field B_0. The black arrow shows the vein which is clearly seen in the tSWI (Fig. 7f). In SWI (Fig. 7e), the vein actually shows a dark structure which is in fact more associated with its edges. This makes the veins appear much bigger in the SWI than in the tSWI data, as can be seen from the minimum intensity projections (mIPs) in Fig. 7g,h. This nonlocal phase information used in SWI can lead to an inaccurate estimation of the geometry of microbleeds, as demonstrated in Fig. 8. In this TBI case, tSWI has more faithfully represented the microbleeds.

DISCUSSION

Quantitative susceptibility mapping offers an additional means to recognize veins and microbleeds and other tissues with high iron content as phase imaging does. However, the phase images are dependent on each object's shape and orientation, while the susceptibility values of the structures are not, at least in principle. Therefore, to produce better susceptibility-weighted images we investigated the use of susceptibility maps for the masking process.
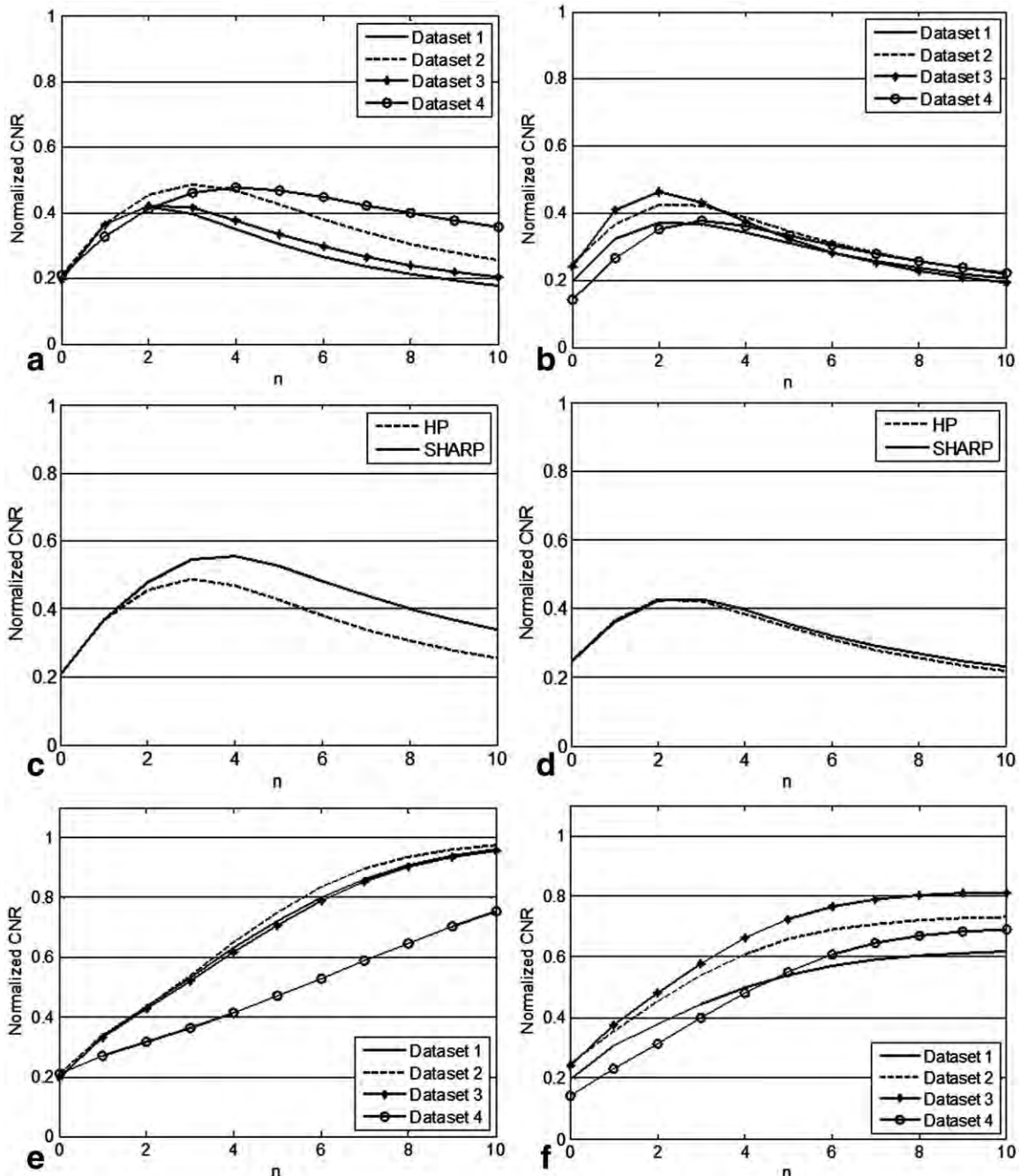
Figure 5. Local CNRs of the right septal vein (**a,c,e**) and the left internal cerebral vein (**b,d,f**) from different datasets with anisotropic resolution. **a–d**: Generated when threshold $\chi_1 = 0$ was used to create the susceptibility weighting masks, while **e,f** were generated when $\chi_1 = 3\sigma_\chi$ was used. The CNRs were normalized by the corresponding SNRs listed in Table 2. **c,d**: The CNRs of the two veins in Dataset 2 with anisotropic resolution, when different data processing methods were used for susceptibility mapping (see Fig. 6 for examples of the tSWI images).

There are a number of key observations that can be made from the data presented herein. First, the results presented in this article demonstrate that the object shape and orientation can be reasonably accounted for by using susceptibility maps and, hence, the inability of SWI processing to enhance veins at different orientations can be overcome. Besides, the blooming artifact due to the dipolar phase of microbleeds in conventional SWI was avoided. This leads to potential applications of this technique, for example, the evaluation of microbleeds

in TBI studies. Second, tSWI can be used to process isotropic data, whereas SWI processing has relied on anisotropic data for its best results due to the direct use of phase information, which is orientation-dependent (6). In the past, SWI data have usually been collected with anisotropic resolution with 2 mm slice thickness (6). However, modern segmented echo planar approaches are becoming viable and one expects to see more data being collected with isotropic voxel sizes (19,20). The high isotropic resolution also helps to reduce the error caused by the partial

Table 2

Local CNRs of the Two Selected Veins on tSWI Images, SWI Images and the Original Magnitude Images, as Well as the SNRs in the Original Magnitude Images From Different Datasets

			Isotropic case		Anisotropic case	
			Vein 1	Vein 2	Vein 1	Vein 2
Dataset 1	CNR	tSWI	0.6	0.5	0.4	0.4
		SWI	0.2	0.1	0.3	0.1
		Mag	0.2	0.1	0.2	0.2
	SNR		10.1		18.8	
Dataset 2	CNR	tSWI	0.7	0.5	0.5	0.4
		SWI	0.1	0.1	0.3	0.2
		Mag	0.2	0.2	0.2	0.2
	SNR		9.7		17.0	
Dataset 3	CNR	tSWI	0.7	0.6	0.4	0.5
		SWI	0.1	0.2	0.3	0.2
		Mag	0.2	0.3	0.2	0.2
	SNR		9.1		17.0	
Dataset 4	CNR	tSWI	0.6	0.5	0.4	0.4
		SWI	0.2	0.1	0.3	0.1
		Mag	0.3	0.2	0.2	0.1
	SNR		9.4		18.6	

The CNRs were normalized by the corresponding SNRs. The SNRs were measured from the reference regions close to the right septal vein in the magnitude images. The tSWI images were generated using $\chi_1 = 0$, $\chi_2 = 0.45$ppm, $n = 2$.

voluming effects in susceptibility quantification, and thus leads to improved quality for tSWI. Note that high image resolution will also lead to lower SNR within a given image time and thus lower CNR. Generally speaking, tSWI is most advantageous with the isotropic datasets. Third, the use of a susceptibility mask is not restricted to the paramagnetic venous blood, but it could also be designed to study the diamagnetic materials (e.g., calcifications, which have negative susceptibility in the susceptibility maps). Fourth, the effects of the upper and lower thresholds used in creating the susceptibility masks have been studied for two reasonable values, and the optimal number of multiplications, n, has been determined. When the lower threshold was set to zero, the fact that a continuous mask from zero to unity is generated makes it possible to enhance contrast even in smaller veins, or larger veins that have had their phase artificially suppressed by using the highpass filter, or in structures that have lower iron content. The use of $\chi_1 = 3\sigma_\chi$ helps to avoid amplifying noise in regions of low susceptibility and hence leads to a higher CNR. However, at the same time it can prevent small veins or structures with very low susceptibility from being enhanced. In addition, different datasets require different optimal n values. To avoid this problem, it may be more practical to choose χ_1 to be 0. We choose the upper threshold χ_2 to be 0.45 ppm, as it corresponds to the theoretical susceptibility of venous blood when the oxygen saturation is 70% and the hematocrit is 45%. Increasing this upper threshold may lead to a slightly larger value for the optimal n when the susceptibility value of the vein is much
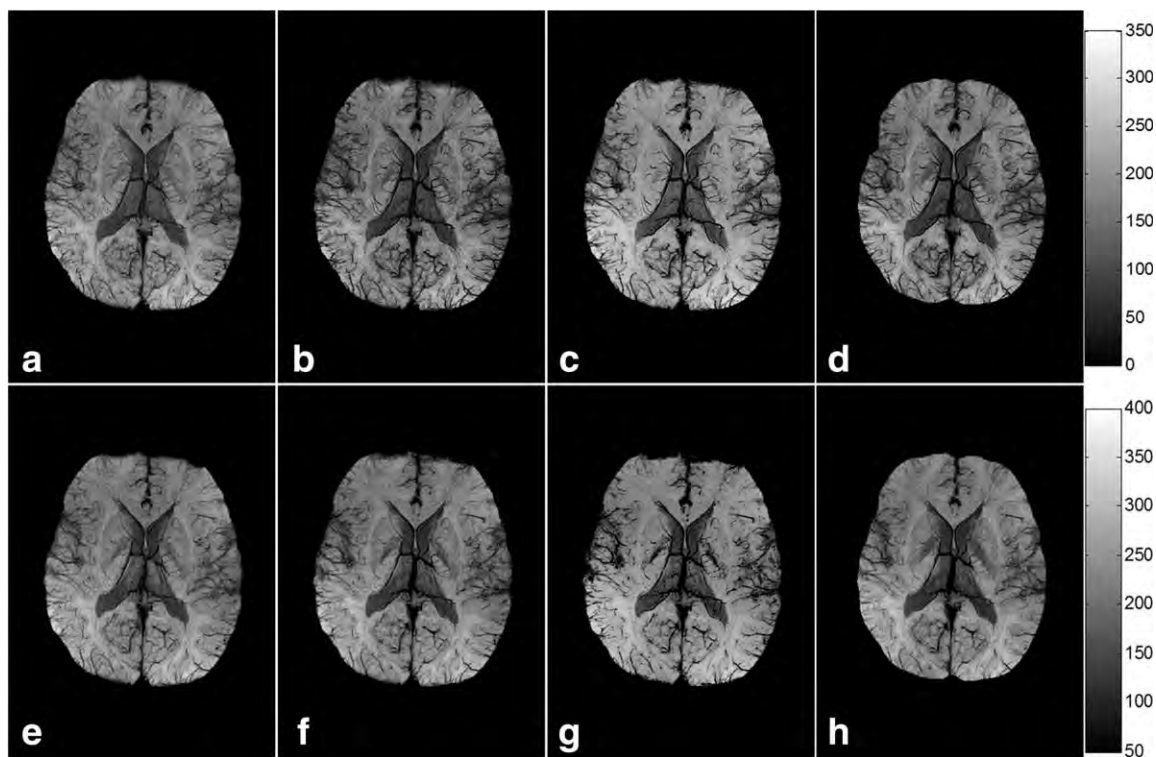

Figure 6. Comparison between mIPs of tSWI and SWI data over 16 mm for isotropic (top row) and anisotropic data (bottom row) for Dataset 2. For (**b,c,f,g**), susceptibility maps were generated using homodyne highpass filtering and thresholded k-space division; while for (**d,h**), susceptibility maps were generated using SHARP and geometry constrained iterative algorithm. (**a**) isotropic SWI mIP; (**b**) isotropic tSWI mIP ($\chi_1 = 0$, $\chi_2 = 0.45$ ppm, $n = 2$); (**c**) isotropic tSWI mIP ($\chi_1 = 3\sigma_\chi$, $\chi_2 = 0.45$ ppm, $n = 4$); (**d**) isotropic tSWI mIP ($\chi_1 = 0$, $\chi_2 = 0.45$ ppm, $n = 2$); (**e**) anisotropic SWI mIP. (**f**) anisotropic tSWI mIP ($\chi_1 = 0$, $\chi_2 = 0.45$ ppm, $n = 2$). (**g**) anisotropic tSWI mIP ($\chi_1 = 3\sigma_\chi$, $\chi_2 = 0.45$ ppm, $n = 8$). (**h**) anisotropic tSWI mIP ($\chi_1 = 0$, $\chi_2 = 0.45$ ppm, $n = 2$).
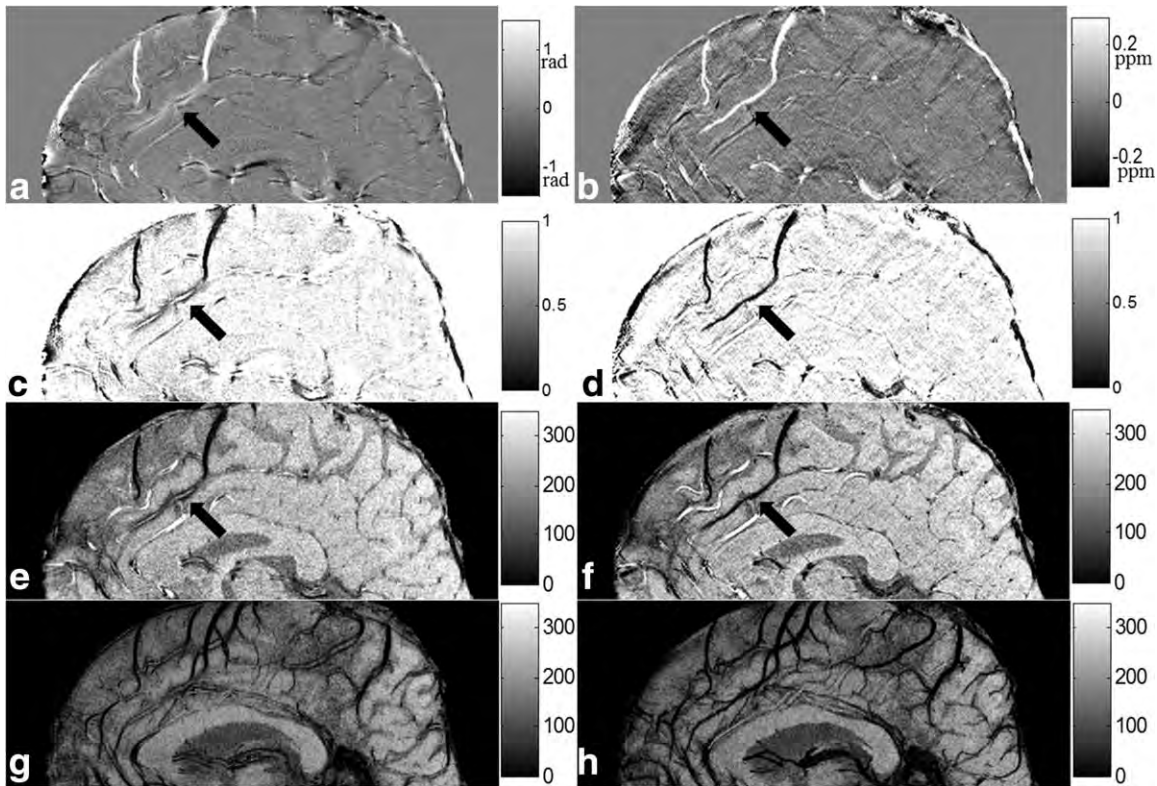
Figure 7. A sagittal view showing a vein near the magic angle (54.7° relative to the main magnetic field) as indicated by the black arrows. (**a**) Phase image (from a left-handed system) showing effectively zero phase inside the vein, with outer field dipole effects also visible; (**b**) susceptibility maps showing the vein as uniformly bright; (**c**) susceptibility weighting mask obtained from the phase image ($n = 4$); (**d**) susceptibility weighting mask obtained from the susceptibility maps ($\chi_1 = 0$, $\chi_2 = 0.45$ ppm, $n = 2$); (**e**) SWI showing unsuppressed signal inside the vein; and (**f**) tSWI showing a clear suppression of the vein even at the magic angle. (**g**) mIP of SWI in the sagittal direction. (**h**) mIP of tSWI in the sagittal direction. Note the vessels near the magic angle are now well delineated in the tSWI data.

smaller than χ_2. In most cases, $n = 2$ gave optimal results, for $\chi_1 = 0$ and $\chi_2 = 0.45$ ppm. In order to capture smaller veins or structures with lower suscepti-bility values such as the basal ganglia, a slightly larger n can be used for either isotropic or anisotropic datasets. The lower susceptibility values are due to a
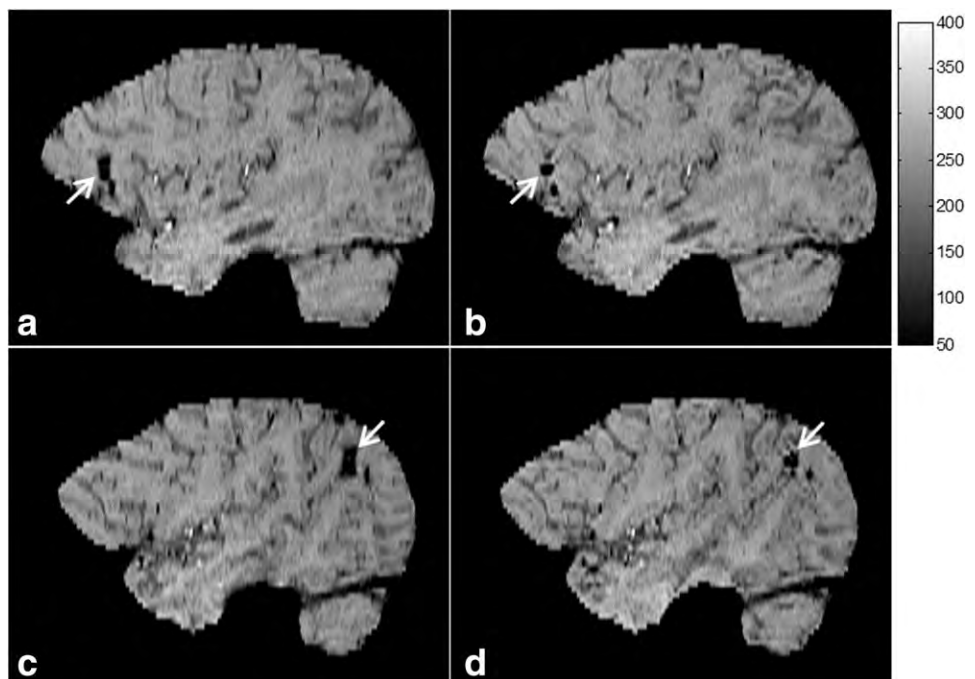

Figure 8. Sagittal views of SWI (**a,c**) and tSWI images (**b,d**) in a TBI case. The micro-bleeds appear much bigger on the SWI images than on the tSWI images, as indicated by the white arrows. This is due to the nonlocal phase information used in the conventional SWI weighting mask. For better visualization, the images were interpolated in through-plane direction from a resolution of $0.5 \times 0.5 \times 2$ mm^3 to 0.5 mm isotropic resolution.

combined effect of partial voluming and highpass filtering. Fifth, the predicted CNRs slightly deviate from measured CNRs in simulations, as the mean value of the susceptibility mask W in the background reference region is slightly less than 1. As a result, this creates slight differences between the prediction and measurements at large n values ($n > 4$). Lastly, conventional SWI uses phase information which is dependent on echo time and usually a relatively long echo time is used in SWI data collection. Although the phase mask could be redefined as a function of echo time to accommodate the loss of phase information as echo times are reduced, no such modification needs to take place for tSWI since the susceptibility map does not change with echo time. However, when echo times are reduced, the phase SNR used to generate the susceptibility map will decrease. On the other hand, if echo times become too long, phase aliasing occurs and the apparent size of the vessel will increase. Thus, tSWI makes the use of short echo times possible as long as the SNR is high enough to create a reasonable estimate of the local susceptibilities. The selection of a shorter TE has several major advantages, including reducing background field induced phase artifacts, shorter scan time, and better overall image quality.

There are several limitations to this method. First, we are using susceptibility maps generated from a single orientation dataset to create the mask for tSWI. These susceptibility maps can have streaking artifacts which are caused by the singularities in the inverse kernel (7–15). The streaking artifacts could permeate the tSWI data causing artifacts that did not exist before or decrease the CNR of gray matter structures. Some newer techniques such as nonlinear regularization (10,13,14) and iterative algorithms (8) will reduce the streaking artifacts and the latter is particularly time-efficient. Another common problem of the single orientation QSM method is the systematic underestimation or bias of the susceptibility. However, this can be compensated by the thresholds used to generate the tSWI weighting masks. Second, we used the traditional homodyne highpass filter to remove the background phase artifacts in the in vivo data. Even though homodyne highpass filtering could be applied without phase unwrapping, it leads to an underestimation of the susceptibility, especially for large objects. This can be improved by using newly developed background field removal methods (9,21). But for relatively small structures such as veins, homodyne highpass filtering already gives satisfying results. Given the fact that homodyne highpass filtering is still being widely used, the proposed algorithm can be directly added to the current SWI data processing scheme.

In conclusion, we have proposed a data processing scheme which we refer to as true SWI or tSWI to generate SWI-like images using susceptibility maps. This helps to avoid the orientation dependence related problem in SWI, especially in data with isotropic resolution and, in the future, possibly to allow the use of short TE SWI data collection. This tSWI data provide better and more consistent visualization of the venous system and thus have potential clinical applications in the study of neurodegenerative diseases.

REFERENCES

1. Haacke EM, Xu Y, Cheng YN, Reichenbach JR. Susceptibility weighted imaging (SWI). Magn Reson Med 2004;52:612–618.
2. Mittal S, Wu Z, Neelavalli J, Haacke EM. Susceptibility-weighted imaging: technical aspects and clinical applications, Part 2. AJNR Am J Neuroradiol 2009;30:232–252.
3. Haacke EM, Reichenbach JR (eds.). Susceptibility weighted imaging in MRI: basic concepts and clinical applications, 1st ed. New York: Wiley-Blackwell; 2011.
4. Haacke EM, Brown RW, Thompson MR, Venkatesan R. Magnetic resonance imaging: physical principles and sequence design, 1st ed. New York; Wiley-Liss; 1999.
5. Marques JP, Bowtell R. Application of a Fourier-based method for rapid calculation of field inhomogeneity due to spatial variation of magnetic susceptibility. Concepts Magn Reson B Magn Reson Eng 2005;25B:65–78.
6. Xu Y, Haacke EM. The role of voxel aspect ratio in determining apparent vascular phase behavior in susceptibility weighted imaging. Magn Reson Imaging 2006;24:155–160.
7. Haacke EM, Tang J, Neelavalli J, Cheng YC. Susceptibility mapping as a means to visualize veins and quantify oxygen saturation. J Magn Reson Imaging 2010;32:663–676.
8. Tang J, Liu S, Neelavalli J, Cheng YCN, Buch S, Haacke EM. Improving susceptibility mapping using a threshold-based k-space/image domain iterative reconstruction approach. Magn Reson Med 2013;69:1396–1407.
9. Schweser F, Deistung A, Lehr BW, Reichenbach JR. Quantitative imaging of intrinsic magnetic tissue properties using MRI signal phase: an approach to in vivo brain iron metabolism? NeuroImage 2011;54:2789–2807.
10. Schweser F, Sommer K, Deistung A, Reichenbach JR. Quantitative susceptibility mapping for investigating subtle susceptibility variations in the human brain. Neuroimage 2012;62:2083–2100.
11. Shmueli K, de Zwart JA, van Gelderen P, Li T, Dodd SJ, Duyn JH. Magnetic susceptibility mapping of brain tissue in vivo using MRI phase data. Magn Reson Med 2009;62:1510–1522.
12. Liu T, Spincemaille P, de Rochefort L, Kressler B, Wang Y. Calculation of susceptibility through multiple orientation sampling (COSMOS): a method for conditioning the inverse problem from measured magnetic field map to susceptibility source image in MRI. Magn Reson Med 2009;61:196–204.
13. Liu J, Liu T, de Rochefort L, et al. Morphology enabled dipole inversion for quantitative susceptibility mapping using structural consistency between the magnitude image and the susceptibility map. Neuroimage 2012;59:2560–2568.
14. De Rochefort L, Liu T, Kressler B, et al. Quantitative susceptibility map reconstruction from MR phase data using Bayesian regularization: Validation and application to brain imaging. Magn Reson Med 2010;63:194–206.
15. Wharton S, Bowtell R. Whole-brain susceptibility mapping at high field: a comparison of multiple- and single-orientation methods. NeuroImage 2010;53:515–525.
16. Jain V, Abdulmalik O, Propert KJ, Wehrli FW. Investigating the magnetic susceptibility properties of fresh human blood for non-invasive oxygen saturation quantification. Magn Reson Med 2012;68:863–867.
17. Smith SM. Fast robust automated brain extraction. Hum Brain Mapp 2002;17:143–155.
18. Abdul-Rahman HS, Gdeisat MA, Burton DR, Lalor MJ, Lilley F, Moore CJ. Fast and robust three-dimensional best path phase unwrapping algorithm. Appl Opt 2007;46:6623–6635.
19. Xu Y, Haacke EM. An iterative reconstruction technique for geometric distortion-corrected segmented echo-planar imaging. Magn Reson Imaging 2008;26:1406–1414.
20. Zwanenburg JJM, Versluis MJ, Luijten PR, Petridou N. Fast high resolution whole brain T2* weighted imaging using echo planar imaging at 7T. Neuroimage 2011;56:1902–1907.
21. Liu T, Khalidov I, de Rochefort L, et al. A novel background field removal method for MRI using projection onto dipole fields (PDF). NMR Biomed 2011;24:1129–1136.